

A multidisciplinary approach to quantify the permeability of the Whakaari/White Island volcanic hydrothermal system (Taupo Volcanic Zone, New Zealand)

Michael J. Heap ^{a,*}, Ben M. Kennedy ^b, Jamie I. Farquharson ^a, James Ashworth ^c, Klaus Mayer ^d, Mark Letham-Brake ^e, Thierry Reuschlé ^a, H. Albert Gilg ^f, Bettina Scheu ^d, Yan Lavallée ^c, Paul Siratovich ^b, Jim Cole ^b, Arthur D. Jolly ^g, Patrick Baud ^a, Donald B. Dingwell ^d

^a Géophysique Expérimentale, Institut de Physique de Globe de Strasbourg (UMR 7516 CNRS, Université de Strasbourg/EOST), 5 rue René Descartes, 67084 Strasbourg cedex, France

^b Geological Sciences, University of Canterbury, Private Bag 4800, 8140 Christchurch, New Zealand

^c Earth, Ocean and Ecological Sciences, University of Liverpool, Liverpool L69 3GP, United Kingdom

^d Earth & Environmental Sciences, Ludwig-Maximilians-Universität, Theresienstr. 41/III, 80333 Munich, Germany

^e Kakapo Disaster Resilience, 2/48 Brockworth Place, Riccarton, 8011 Christchurch, New Zealand

^f Lehrstuhl für Ingenieurgeologie, Technische Universität München, Arcisstr. 21, 80333 Munich, Germany

^g GNS Science, 1 Fairway Avenue, Avalon, 5040, New Zealand

ARTICLE INFO

Article history:

Received 23 June 2016

Received in revised form 7 October 2016

Accepted 12 December 2016

Available online 14 December 2016

Keywords:

Alteration

Fracture

Porosity

Permeability

Lava

Tuff

Pore pressure

ABSTRACT

Our multidisciplinary study aims to better understand the permeability of active volcanic hydrothermal systems, a vital prerequisite for modelling and understanding their behaviour and evolution. Whakaari/White Island volcano (an active stratovolcano at the north-eastern end of the Taupo Volcanic Zone of New Zealand) hosts a highly reactive hydrothermal system and represents an ideal natural laboratory to undertake such a study. We first gained an appreciation of the different lithologies at Whakaari and (where possible) their lateral and vertical extent through reconnaissance by land, sea, and air. The main crater, filled with tephra deposits, is shielded by a volcanic amphitheatre comprising interbedded lavas, lava breccias, and tuffs. We deployed field techniques to measure the permeability and density/porosity of (1) >100 hand-sized sample blocks and (2) layered unlithified deposits in eight purpose-dug trenches. Our field measurements were then groundtruthed using traditional laboratory techniques on almost 150 samples. Our measurements highlight that the porosity of the materials at Whakaari varies from ~0.01 to ~0.7 and permeability varies by eight orders of magnitude (from $\sim 10^{-19}$ to $\sim 10^{-11} \text{ m}^2$). The wide range in physical and hydraulic properties is the result of the numerous lithologies and their varied microstructures and alteration intensities, as exposed by a combination of macroscopic and microscopic (scanning electron microscopy) observations, quantitative mineralogical studies (X-ray powder diffraction), and mercury porosimetry. An understanding of the spatial distribution of lithology and alteration style/intensity is therefore important to decipher fluid flow within the Whakaari volcanic hydrothermal system. We align our field observations and porosity/permeability measurements to construct a schematic cross section of Whakaari that highlights the salient findings of our study. Taken together, the alteration typical of a volcanic hydrothermal system can result in increases (due to alteration-induced dissolution and fracturing) and decreases (due to hydrothermal precipitation) to permeability. Importantly, a decrease in permeability—be it due to fracture sealing in lava, pore-filling alunite precipitation in tuff, near-vent cementation by sulphur, and/or well-sorted layers of fine ash—can result in pore pressure augmentation. An increase in pore pressure could result in ground deformation, seismicity, jeopardise the stability of the volcanic slopes, and/or drive the wide variety of eruptions observed at Whakaari. Our systematic study offers the most complete porosity-permeability dataset for a volcanic hydrothermal system to date. These new data will inform and support modelling, unrest monitoring, and eruption characterisation at Whakaari and other hydrothermally modified volcanic systems worldwide.

© 2016 Elsevier B.V. All rights reserved.

1. Introduction

The permeability of the materials within a volcanic hydrothermal system controls the ease at which exsolved magmatic volatiles can

* Corresponding author.

E-mail address: heap@unistra.fr (M.J. Heap).

escape the magma-filled conduit (Eichelberger et al., 1986; Jaupart, 1998; Collinson and Neuberg, 2012), as well as the ingress, circulation, and interaction of meteoric and/or marine (in the case of volcanic islands, coastal, or submarine volcanoes) water and hydrothermal fluids (Bibby et al., 1995; Edmonds et al., 2003; Rowland and Sibson, 2004; Hurwitz et al., 2007). The permeability of a volcanic hydrothermal system therefore exerts a first-order control on the magnitude and distribution of pore pressure (Hurwitz et al., 2007; Todesco et al., 2010; Fournier and Chardot, 2012). The build-up of pore pressure within a volcanic hydrothermal system can lead to catastrophic flank collapse (Day, 1996; Voight and Elsworth, 1997; Reid et al., 2001; Reid, 2004; Moon et al., 2009; Procter et al., 2014), seismicity (Nishi et al., 1996; Sherburn et al., 1998; Bean et al., 2014; Chardot et al., 2015), and/or drive a wide variety of eruptions, from phreatic (Barberi et al., 1992; Kaneshima et al., 1996; Christenson et al., 2010; Mayer et al., 2015; Montanaro et al., 2016; Mayer et al., 2016a, 2016b) and phreatomagmatic (Bertagnini et al., 1991; Houghton and Nairn, 1991) explosions to larger, more sustained eruptions (Houghton and Nairn, 1991; Christenson, 2000; Deino et al., 2004). Detailed knowledge of the permeability of the materials found within hydrothermal systems will therefore provide a deeper understanding of their behaviour and evolution (Hurwitz et al., 2007; Collombet, 2009; Todesco et al., 2010; Christenson et al., 2010; Fournier and Chardot, 2012; Collinson and Neuberg, 2012).

While laboratory studies have exposed porosity-permeability relationships for a variety of volcanic rocks (Klug and Cashman, 1996; Saar and Manga, 1999; Rust and Cashman, 2004; Mueller et al., 2005; Wright et al., 2009; Farquharson et al., 2015; Kushnir et al., 2016; Wadsworth et al., 2016; Heap and Kennedy, 2016), studies that provide values of permeability for the highly altered lithologies that typically comprise hydrothermal systems are scarce (Saratovich et al., 2014; Mayer et al., 2016a, 2016b), largely due to their microstructural complexity and variability. To emphasise, hydrothermal alteration can be the result of dissolution, mineral precipitation, and secondary mineralisation (Browne, 1978) and can therefore result in increases or decreases in porosity, a physical property known to exert a first-order control on permeability (e.g., Bourbié and Zinszner, 1985). For example, the hydrothermal alteration of volcanic rocks can replace the existing minerals with weak minerals such as clays (e.g., kaolinite, illite, and smectite; Steiner, 1968; Browne, 1978; Inoue, 1995) and sulphates (e.g., alunite and jarosite; Johnston, 1977; Ece et al., 2008), leading to material weakening (del Potro and Hürlimann, 2009; Pola et al., 2012, 2014; Frolova et al., 2014; Wyering et al., 2014, 2015; Heap et al., 2015a), fracturing/disintegration, and therefore an increase in permeability. On the other hand, hydrothermal alteration can infill pores and fractures (both micro- and macrofractures) with precipitated minerals (Edmonds et al., 2003; Wyering et al., 2014; Heap et al., 2015a; Ball et al., 2015) leading to reductions in permeability (e.g., Griffiths et al., 2016). The type and intensity of hydrothermal alteration will not only depend on the rock type, but also on the temperature (Wyering et al., 2014; Frolova et al., 2014) and composition (including pH) of the circulating fluids, and the effective fluid-rock ratio (Browne, 1978; Reed, 1997), factors that can vary tremendously in both space and time. The consequence of this variability is that the rocks within a volcanic hydrothermal system will suffer a broad array of chemical alteration that will modify their physical properties, such as porosity and permeability, in different ways and to different degrees.

And so it is that, especially for volcanic hydrothermal systems, an understanding of their permeability—and therefore behaviour—must rely on a detailed comprehension of the variability in porosity and permeability of the accumulated materials, and information as to their spatial distribution. Whakaari volcano (an active stratovolcano located at the north-eastern end of the Taupo Volcanic Zone of New Zealand) hosts an open, highly reactive hydrothermal system (hot springs and mud pools, fumaroles, acid streams and lakes) (Giggenbach et al., 2003 and references therein) and represents an ideal natural laboratory to undertake such a study. We present herein a multidisciplinary study

designed to better understand the permeability of an active volcanic hydrothermal system. One of the primary goals of this contribution is to produce a very large dataset to inform future modelling efforts. The permeability of the materials within active volcanic hydrothermal systems is, for example, required to understand and accurately model the outgassing of magmatic volatiles from the magma-filled conduit (Collombet, 2009; Collinson and Neuberg, 2012), subsurface hydrothermal activity and therefore volcanic unrest (Hurwitz et al., 2007; Peltier et al., 2009; Todesco et al., 2010; Christenson et al., 2010; Fournier and Chardot, 2012; Christenson et al., 2016), gas monitoring (Bloomberg et al., 2014; Peiffer et al., 2014), and volcano seismicity (Leet, 1988; Nishi et al., 1996; Sherburn et al., 1998; Bean et al., 2014; Chardot et al., 2015).

2. Whakaari (White Island volcano)

Whakaari is an active andesitic-dacitic stratovolcano located 48 km north of New Zealand's North Island, at the north-eastern end of the Taupo Volcanic Zone (Fig. 1). The island, the tip of a much larger submarine structure, summits at 321 m above sea level and measures 2.4 km east-west by 2 km north-south (Clark and Cole, 1986; Houghton and Nairn, 1991 and references therein). Whakaari's subaerial structure consists of two cones: the extinct and partially eroded Ngatoro Cone and the active, amphitheatre-shaped Central Cone (Fig. 1). Both are constructed from lavas, tuffs, agglomerates, tephra, dykes, and breccias (Cole et al., 2000 and references therein). Geomorphic evidence suggests that 0.21 km³ of material was prehistorically removed from the Central Cone due to major flank failures involving weak hydrothermally altered rock (Moon et al., 2009).

Whakaari hosts an open, highly reactive hydrothermal system that has existed for approximately 10,000 years (Giggenbach et al., 2003 and references therein). The mélange of marine/meteoric water and hot magmatic fluids generate acid brines (Giggenbach et al., 2003 and references therein; Christenson et al., 2016) that rise to the surface forming hot springs, mud pools, fumaroles, and acid streams and lakes. The pH of the acid streams can be as low as ~2 (Hedenquist et al., 1993; Donachie et al., 2002). Crater lake, a large lake of boiling acidic waters in the western subcrater, which appears to vary in volume due to meteorological conditions and fluctuating levels of hydrothermal activity (Christenson et al., 2016), is the focus of present day volcanic activity and outgassing (e.g., Werner et al., 2008; Bloomberg et al., 2014), although more diffuse outgassing through the crater floor and outgassing through fumaroles that line the crater rim is also observed (Bloomberg et al., 2014).

Volcanic eruptions at Whakaari are generally phreatic or phreatomagmatic in style (although Strombolian activity occurred from the late seventies to the mid-eighties; Houghton and Nairn, 1991), and form discrete craters within the main crater-fill deposits of the Central Cone (Houghton and Nairn, 1991; Cole et al., 2000). Indeed, a minimum of 28 phreatic or phreatomagmatic eruptions has occurred since 1826 (Mayer et al., 2015). Prehistoric eruptions at Whakaari, recorded in the stratigraphy of crater walls of the Central Cone, were characterised by the extrusion of lava (Cole et al., 2000). Eruptions at Whakaari are frequent to this day, the most recent occurring on April 27, 2016.

Geophysical surveys on main crater floor highlight ground deformation episodes within the recently formed eruption centres and fumarole fields, interpreted as an increase in pore pressure due to the migration of hydrothermal fluids and/or shallow magma injection (e.g., Peltier et al., 2009; Fournier and Chardot, 2012) and/or lake level variations (Christenson et al., 2016). The circulation of hydrothermal fluids within these zones has been blamed for swarms of low-amplitude, high-frequency earthquakes and volcanic tremors (Nishi et al., 1996; Sherburn et al., 1998; Chardot et al., 2015). Although the permeability of the main crater floor has been inferred from thermal infrared mapping (Mongillo and Wood, 1995) and gas and heat flux mapping (Bloomberg et al., 2014), a systematic study that provides direct measurements of permeability, to our knowledge, is not currently available.

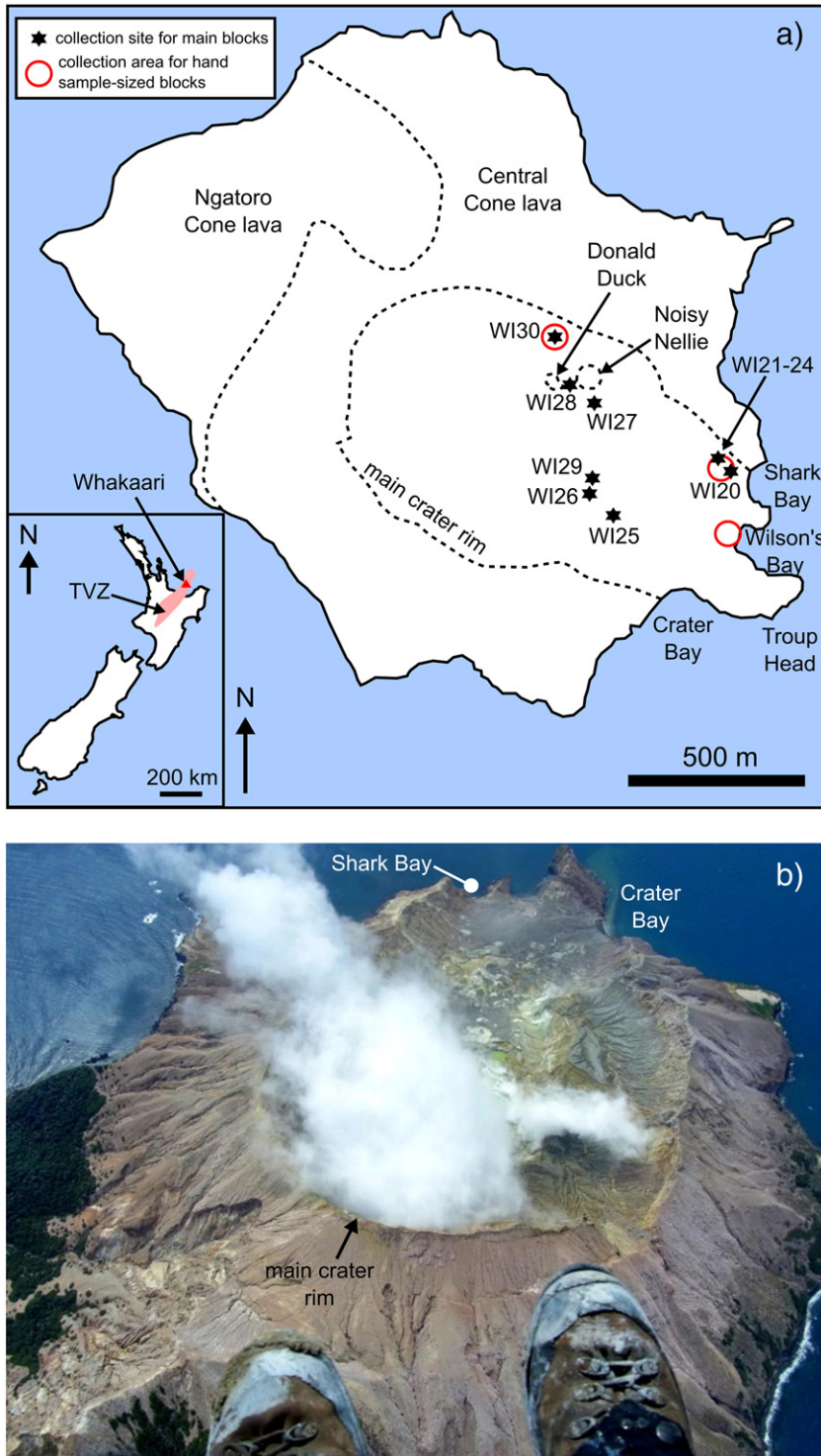


Fig. 1. Whakaari (White Island volcano). (a) Map of Whakaari showing the locations of the collection sites for the lithified materials. The collection areas for the hand-sized sample blocks are indicated by the red circles. The collection sites for the nine main blocks of this study (and the two unlithified materials WI27 and WI28) are indicated by the black stars. The inset shows a map of New Zealand showing the location of the Taupo Volcanic Zone (pink area) and Whakaari volcano (red triangle). (b) Aerial photograph of Whakaari taken looking east-southeast. Note: Ben Kennedy's boots do not provide an accurate scale.

3. Reconnaissance of Whakaari by land, sea, and air

In order to assess the lateral and (where possible) vertical extent of the main lithologies at Whakaari, and therefore select the most appropriate rocks for our study, we lean on decades of reconnaissance missions of the island by land, sea, and air (summarised in Fig. 2). We also consulted historical records.

The modern-day crater walls chiefly comprise interbedded coherent (albeit fractured) and brecciated lavas dipping away from the centre of the island. These sequences of interbedded lava and lava breccia deposits can reach >100 m in thickness (Fig. 2, picture 1). Significant debris from the lava breccia deposit from the north-eastern wall of the volcanic amphitheatre (Fig. 2, picture 7) can be seen at the base of the slope (Fig. 3c).

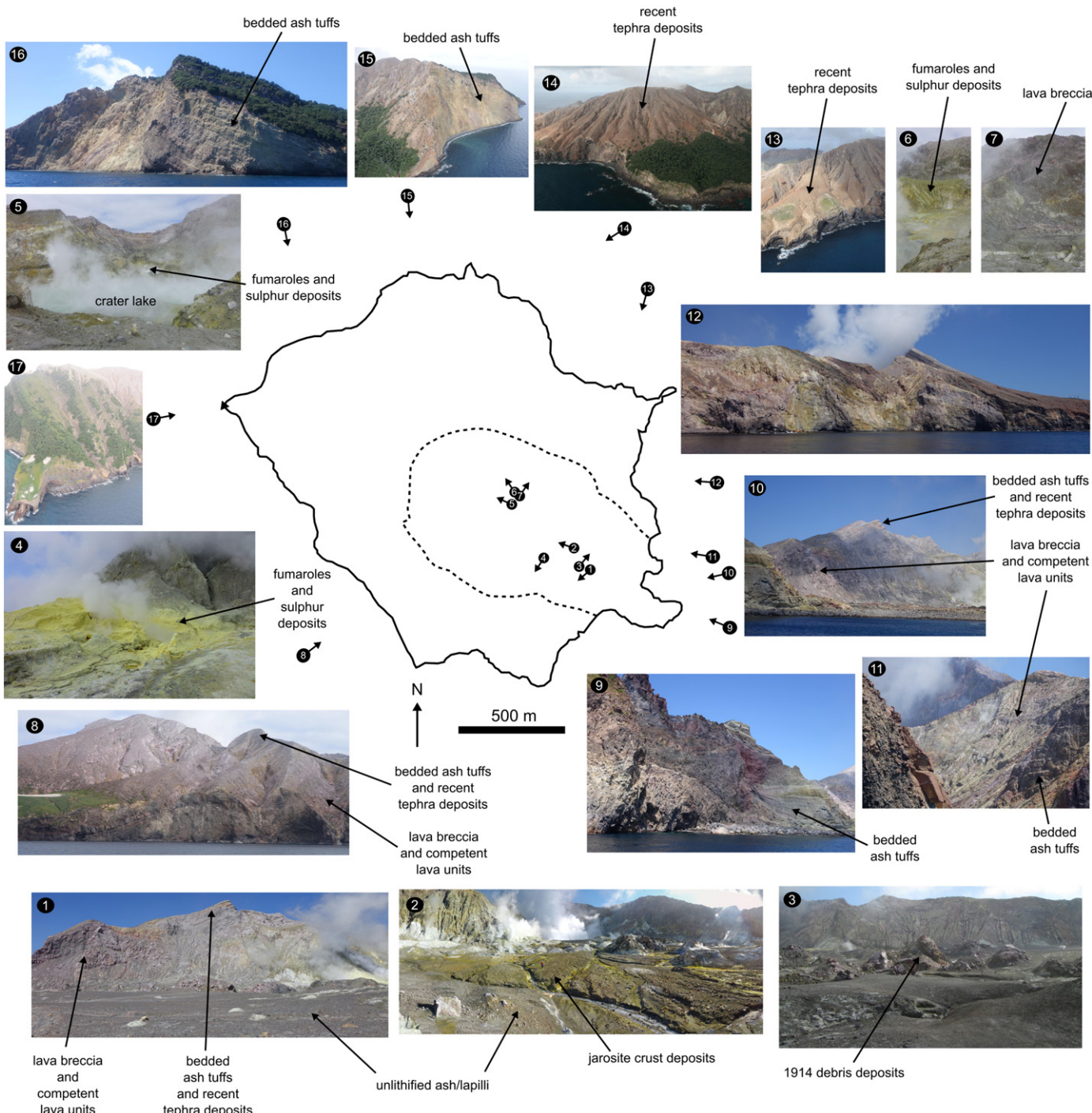


Fig. 2. Reconnaissance by land, sea, and air. Map of Whakaari (centre) surrounded by photographs of the volcanic island. The position from which each photograph was taken and the direction of view are indicated by the numbers and arrows. Prominent rock types are labelled on the photographs.

Interbedded tuffs with a dominantly ash-sized particle size (hereafter called ash tuffs) and coarser lithified pyroclastic deposits (lapilli tuffs) are exposed in perched subcraters within the main crater walls (Fig. 2; pictures 9, 10, and 11) and sequences can reach >10 m in thickness. Bedded sequences of ash and lapilli tuffs, interbedded with the lavas and lava breccias, dip away from the volcano, as seen in the eastern and western sea cliffs of the volcano (Fig. 2; pictures 10, 12, 15, 16). Coarse lithified pyroclastic deposits also fill pre-existing valleys and are exposed in the cliffs on the outer flanks of the volcano.

All of the interbedded deposits forming the crater walls are blanketed by layers of recent tephra deposits comprised of mostly well sorted ash and lapilli airfall (Fig. 2; Fig. 3a–b).

The crater rim is lined with active fumaroles, boiling mud pools, and acid streams (Fig. 2; pictures 2, 4, and 6; Fig. 3d–f). The crater-fill deposits found in these areas have been locally cemented by hydrothermal activity (frequently by sulphur or sulphates), forming lithified crusts (Fig. 2; pictures 2, 4, and 6; Fig. 3d–f). Fumaroles are encrusted by sulphur and sulphur flows are seen—albeit rarely—to extend from fumaroles containing subsurface pools of liquid sulphur (Fig. 3f).

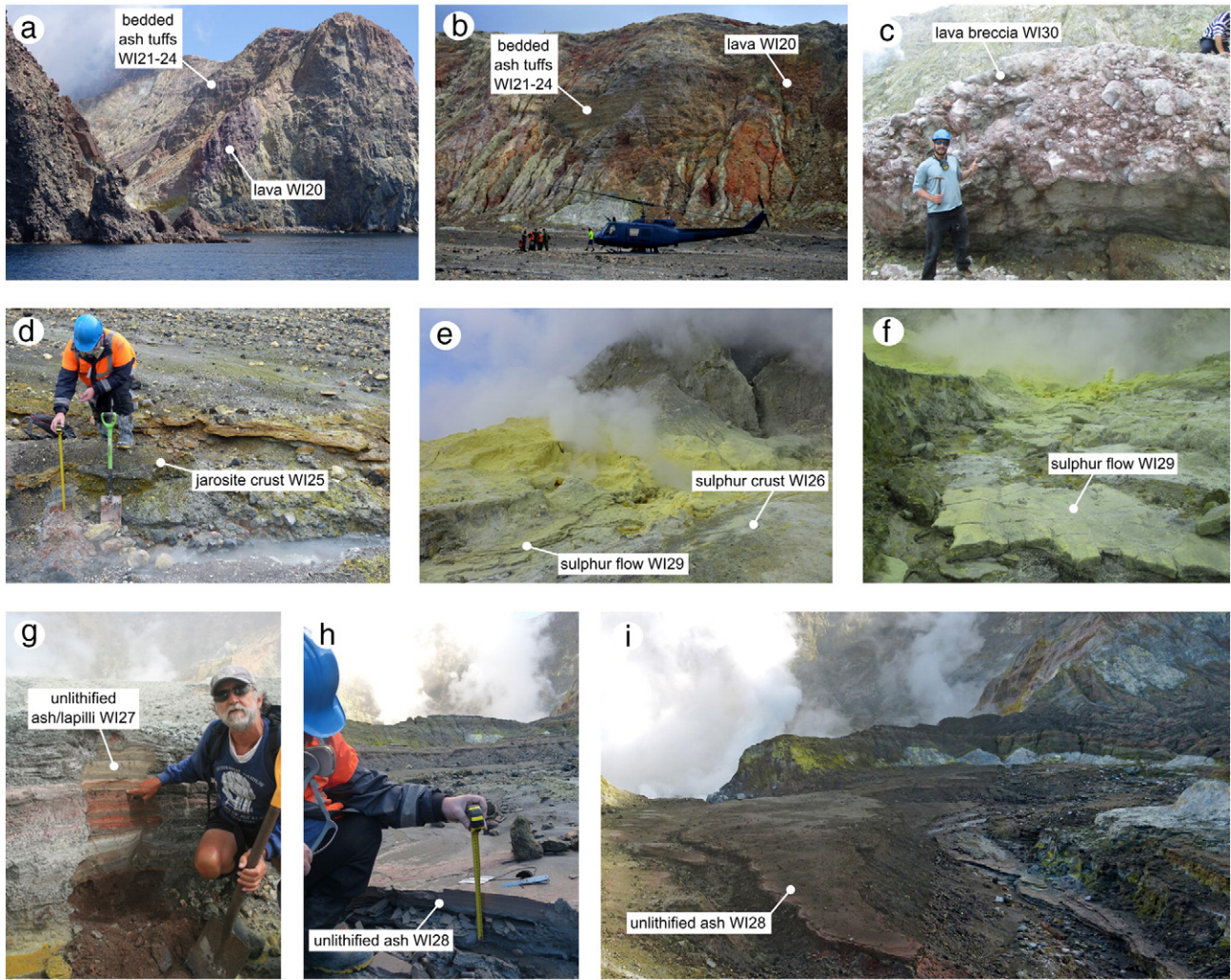


Fig. 3. Photographs showing the sites at which the nine lithified blocks of this study (and the two unlithified materials) were collected. The location of the collection sites are indicated on the map in Fig. 1.

The main crater is filled with unlithified ash and lapilli deposits that are at least several metres in thickness and consist of numerous thin beds (from several mm to several cm in thickness) that can be easily distinguished based on their differences in colour (Fig. 3g). The crater floor is strewn with conspicuous rocky hummocks, the debris from the collapse of the crater wall in September 1914 (Houghton and Nairn, 1991) (Fig. 2, picture 3). Some areas close to the current crater lake—such as the area near Donald Duck and Noisy Nellie craters (Fig. 3h-i)—are blanketed by a well-sorted layer of fine ash ~100 mm in thickness. Eruptions as recent as 2016 have carpeted the crater floor deposits with blocks (Fig. 2; Fig. 3g-i) and poorly sorted surge deposits that have been rapidly reworked into fluvial deposits draining away from the main crater towards the sea (Fig. 2; pictures 2 and 3).

The mapped surface exposure of deposits is further informed by historic accounts, photos, published articles, and volcano monitoring (GeoNet) reports outlining geomorphological changes to the crater. Eruptions have generated ~15 overlapping explosion craters and subsidence pits (up to 200 m deep) in the northern end of the main crater (Houghton and Nairn, 1989) that have been rapidly filled with eruption and erosional debris. Lava is occasionally seen within these craters either as a small dome (Chardot et al., 2015) or as a distinct glow (Houghton and Nairn, 1989). Surges and ballistic debris generate tuff cones (Jolly et al., 2016) in and around the modern crater lake. Debris avalanches, landslides, and rockfalls deposit material on the crater floor and create curvilinear collapse scars in the crater walls

(e.g., Moon et al., 2009). These catastrophic events are further modified by erosion and shifting drainages, as hydrothermal waters make their way south-east towards the ocean via surface streams.

Our reconnaissance has highlighted the extreme complexity and variability of the lithologies that form or are found within the crater at Whakaari. To best capture this variability we chose to (1) collect in excess of a hundred rock blocks for field and laboratory porosity-permeability testing and, (2) perform field porosity-permeability measurements on numerous vertical transects through the unlithified crater floor deposits. We also collected two unlithified crater floor samples for porosity-permeability measurement in the laboratory.

4. Materials and methods for the lithified materials

4.1. Description of the lithified materials

We collected 124 blocks representative of the deposits that form or are found within the crater at Whakaari: 115 hand-sized sample blocks (approximately 100 × 100 × 100 mm, although their shape varied; see Supplementary Figs. S1–S5) and nine larger blocks (approximately 300 × 300 × 300 mm). The hand-sized sample blocks were collected from three sites located within the crater: the accessible scree at (1) the foot of the eastern wall of the volcanic amphitheatre near Shark Bay, (2) Wilson's Bay and, (3) the foot of the northern wall of the volcanic amphitheatre near Noisy Nellie crater (sampling sites are shown on

Fig. 1). These sites were selected due to their accessibility and because they contained blocks representative of the range of materials observed during our reconnaissance ([Figs. 2 and 3](#)). The locations on the volcanic slopes that fed these scree deposits could be readily identified by fresh rockfall scars at each collection site. The blocks consisted of variably altered ash tuffs (i.e., tuffs with an ash-sized particle size), lavas, and lava breccias ([Supplementary Figs. S1–S5](#)). The hand-sized sample blocks were collected for measurements of field density/porosity and permeability and, after coring 20 mm-diameter cylindrical samples from the blocks, measurements of porosity and permeability in the laboratory. The goal of the measurements on the hand-sized sample blocks was to provide a large porosity-permeability dataset; more detailed analyses (scanning electron microscopy (SEM), X-ray powder diffraction (XRPD), and mercury porosimetry) were performed on the nine larger blocks collected. These nine blocks, five of which were used in the recent studies of [Heap et al. \(2015a\)](#) and [Mayer et al. \(2015\)](#), were selected to best represent the variability seen at Whakaari ([Figs. 2 and 3](#)). We collected one block of lava, one block of lava breccia, four blocks of ash tuffs, one block of sulphur flow, one block of sulphur crust, and one block of jarosite crust. Thin sections (double-polished) of each of these rocks were made for SEM analysis and XRPD analysis was performed at the Technische Universität München (TUM, Germany) on powdered material of each of the blocks. For the XRPD analysis, powdered samples were mixed with an internal standard (10% ZnO) and ground for 8 min with 10 ml of isopropyl alcohol in a McCrone Micronising Mill using agate cylinder elements. The XRPD analyses were performed on powder mounts using a PW 1800 X-ray diffractometer (CuK α , graphite monochromator, 10 mm automatic divergence slit, step-scan 0.02° 20° increments per second, counting time 1 s per increment, 40 mA, 40 kV). The crystalline and amorphous phases in the whole rock powders were quantified using the Rietveld program BGMIN ([Bergmann et al., 1998](#)). To confirm the presence of any identified clay minerals, we also separated <2 μm fractions by gravitational settling and prepared oriented mounts that were X-rayed in an air-dried and ethylene glycolated state.

The porphyritic andesite lava (WI20) contains a groundmass of hydrated amorphous glass embedded with phenocrysts and microlites of feldspar and pyroxene. The lava is locally fractured and oxidised ([Fig. 4a](#)). The block was collected at the foot of the eastern wall of the volcanic amphitheatre near Shark Bay ([Figs. 1, 2, and 3a–b](#)) and likely, therefore, originates from one of the competent lava units of the currently active Central Cone ([Cole et al., 2000](#)). Scanning electron microscopy (SEM) has revealed the presence of pervasive microcracking and minor precipitation of alteration minerals (jarosite and gypsum) into some of the pores ([Fig. 4a](#)). The pores are typically a couple of hundred microns in diameter, although some phenocrysts have microporous rims ([Fig. 4a](#)). XRPD analysis highlights the main mineralogical components to be plagioclase (37 wt.%), cristobalite (14 wt.%), amorphous silica (14 wt.%), K-feldspar (14 wt.%), and pyroxene (10 wt%) ([Table 1](#)).

The altered lava breccia collected (WI30) was taken from the deposit shown in [Fig. 3c](#) (located within the debris from the partial collapse of the north-eastern wall of the volcanic amphitheatre ([Fig. 2](#), picture 7)). Although some of the clasts within the deposit were on the order of 1 m ([Fig. 3c](#)), we collected material that contained a maximum clast size of ~10 mm in diameter due to the small size of our laboratory samples (20 mm in diameter). The groundmass of the lava breccia is browned in colour (due to oxidation) and hosts numerous angular lava fragments ([Fig. 4l](#)). SEM analysis shows microcracks, zones of microlitic groundmass, and pores up to 500 μm in diameter ([Fig. 4l](#)). The sample consists of amorphous silica (74 wt.%), kaolinite (10 wt.%), and plagioclase (8 wt%) ([Table 1](#)).

The four ash tuff deposits are composed of partially cemented ash particles, typically altered crystal fragments or completely opalised shards of glass (now composed dominantly of hydrated amorphous silica). The ash tuff blocks collected were selected based on observable differences in colour (alteration type), macroscopic textures

(presence/absence of bedding or laminations), particle size, and degree of cementation. They were all collected in the accessible scree at the foot of the eastern wall of the volcanic amphitheatre near Shark Bay ([Figs. 1, 2, and 3a–b](#)). The ash tuffs can be subdivided into two subgroups: fine-grained white deposits containing pore-filling alunite (WI21 and WI24) and coarser-grained, bedded deposits that do not contain alunite (WI22 and WI23). Of the deposits containing alunite (WI21 and WI24; [Table 1](#)), WI21 contains a lower porosity grey zone ([Fig. 4b](#)) and a higher porosity white zone that contains gas elutriation pipes ([Fig. 4c](#)). All gas elutriation pipes were orientated perpendicular to bedding ([Fig. 4c](#)). WI21 and WI24 contain average particle diameters of ~0.1 and ~0.2 mm, respectively, and an average pore diameter of ~100–200 μm ([Fig. 4b–c and f](#)). Pore-filling alunite ([Fig. 5](#)) likely precipitated following complete devitrification and opal replacement ([Heap et al., 2015a](#)). Of the bedded deposits (WI22 and WI23), the grey-coloured WI22 contains an average particle diameter of ~0.3 mm and 10 mm-thick alternating bands of high- and low-porosity ([Fig. 4d](#)). WI23 contains alternating 3–10 mm-thick alternating brown-red and grey coloured bands ([Fig. 4e](#)). The average particle diameter varies between the different bands in WI23, from ~0.3–0.4 mm in one band to ~0.1 mm in another ([Fig. 4e](#)). Both WI22 and WI23 contain an average pore diameter of ~100–200 μm ([Fig. 4d and e](#)). The mineral composition of all four ash tuffs is given in [Table 1](#). While these tuffs can be described as completely altered (they contain none of their original mineral phases; classified following British Standard practice BS5930, 1999), the presence of alunite attests to the mobility of aluminium and therefore precludes the use of chemical alteration indices such as the Chemical Index of Alteration (CIA), the Chemical Index of Weathering (CIW), and the Plagioclase Index of Alteration (PIA) (see [Pola et al., 2012](#)).

The remaining three lithologies represent those that have been lithified as a result of their proximity to acid streams and fumaroles ([Figs. 2 and 3d–f](#)). They are: sulphur flow, sulphur crust, and jarosite crust. All of these blocks were collected at the south-western margin of the volcanic amphitheatre ([Figs. 2 and 3d–f](#)). The sulphur flow is a very dense rock that forms a layer ~100 mm in thickness located next to an active sulphur fumarole ([Fig. 3f](#)). SEM ([Fig. 4k](#)) and XRPD ([Table 1](#)) analyses shows that the rock comprises few angular ash fragments that are efficiently cemented together by sulphur. Pores are difficult to distinguish, although microcracks are present ([Fig. 4k](#)). The sulphur crust block was collected adjacent to the sulphur flow ([Fig. 3f](#)). The sulphur crust is very heterogeneous and contains ash and lapilli fragments (of devitrified glass, pyroxene, and plagioclase; [Table 1](#)) cemented by sulphur ([Fig. 4h](#)). The sulphur gives the rock its light-green/chartreuse colour. Pores in the sulphur crust are typically ~400–500 μm in diameter ([Fig. 4h](#)). The jarosite crust is similarly heterogeneous, containing ash and lapilli fragments (of devitrified glass, pyroxene, plagioclase, and cristobalite; [Table 1](#)) cemented by jarosite ([Fig. 4g](#)). Pores in the jarosite crust are typically a couple of hundred μm in diameter ([Fig. 4h](#)), but can reach 1 mm in diameter. The mineral composition of all three deposits is given in [Table 1](#).

4.2. Methods for the lithified materials

4.2.1. Field methods

Following several hours of drying in the sun, the permeability of the 115 hand-sized sample blocks was estimated using a portable air permeameter (Vindum Engineering TinyPerm II). The TinyPerm II unit estimates the permeability by evacuating the air from the rock at the nozzle-rock interface (inner diameter of the nozzle = 10 mm) and monitoring the response function of the transient vacuum. The TinyPerm II is a useful field tool that quickly provides an estimate of the permeability of a porous rock, and has been recently used in studies on volcanic materials ([Farquharson et al., 2015](#); [Schaefer et al., 2015](#); [Kendrick et al., 2016](#)). Although the TinyPerm II cannot provide values of permeability below $6.92 \times 10^{-16} \text{ m}^2$, it has been shown to be

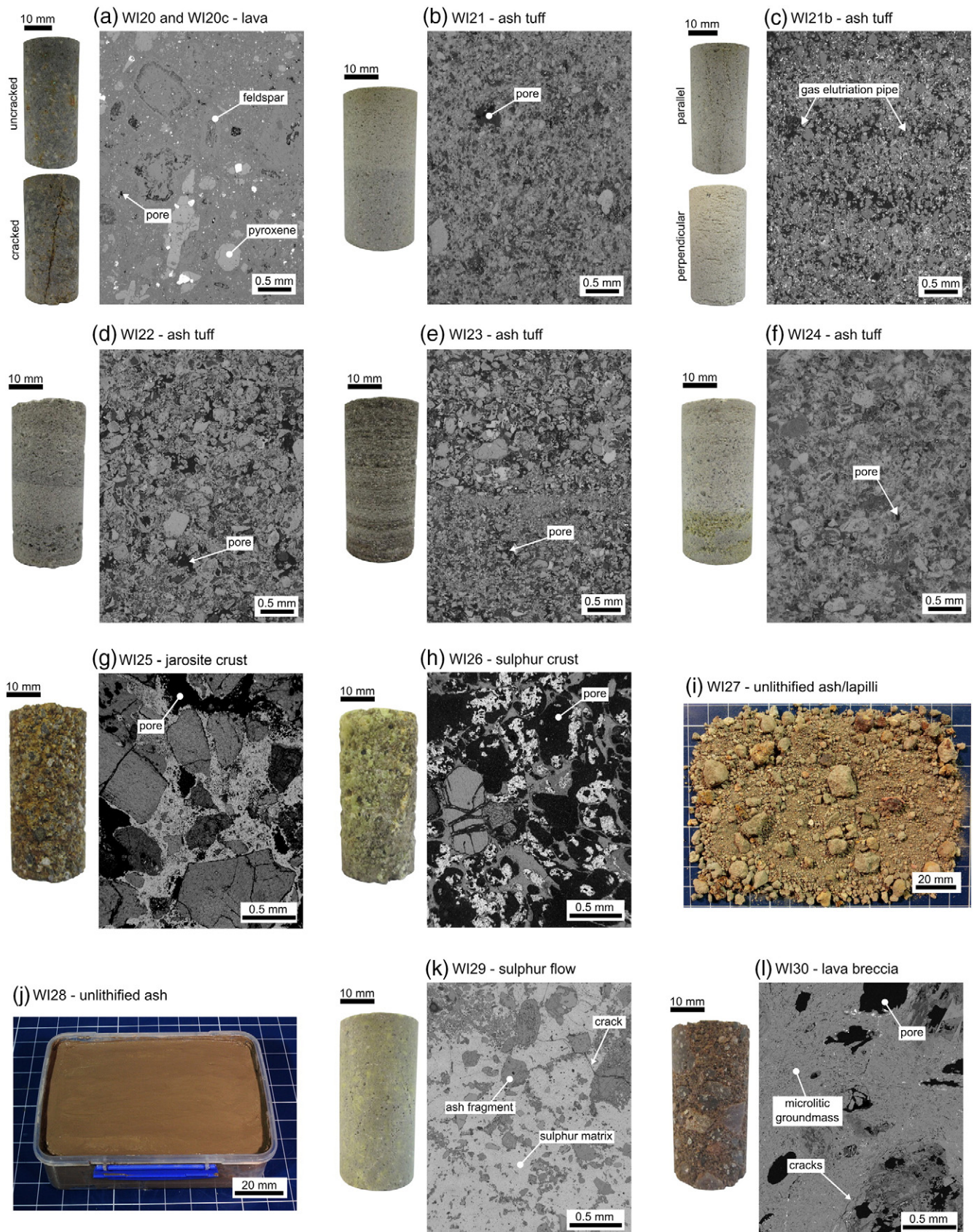


Fig. 4. Photographs and scanning electron microscope (SEM) images of the nine main blocks of this study (and the two unlithified materials). (a) Macrocracked and uncracked lava WI20. (b-f) Ash tuff WI21, WI22, WI23, and WI24. (g) Jarosite crust WI25. (h) Sulphur crust WI26. (i) Unlithified ash/lapilli WI27. (j) Unlithified ash. (k) Sulphur flow WI29. (l) Lava breccia WI30. Collection sites for each material are indicated in Fig. 1 and photographs of the collection sites are provided in Fig. 3.

Table 1

X-ray powder diffraction (XRPD) analysis showing the quantitative bulk mineralogical composition of the nine lithified blocks and the two unlithified samples chosen for additional analyses. Values are in wt.%

Sample name Rock type	WI20 WI20c Lava	WI21 WI21b Ash tuff	WI22 Ash tuff	WI23 Ash tuff	WI24 Ash tuff	WI25 Jarosite crust	WI26 Sulphur crust	WI27 Ash lapilli	WI28 Ash	WI29 Sulphur flow	WI30 Lava breccia
(K, Na)-Alunite	—	32 ± 3	6 ± 3	25 ± 3	1 ± 1	—	—	8 ± 2	—	1 ± 0	—
Jarosite	3 ± 1	—	—	4 ± 1	4 ± 1	25 ± 5	—	—	—	—	1 ± 0
Anhydrite	—	—	—	—	—	—	—	—	—	—	1 ± 0
α-Sulphur	—	—	—	—	—	—	46 ± 5	—	—	99 ± 0	—
Gypsum	4 ± 1	1 ± 1	1 ± 1	—	—	—	—	2 ± 1	3 ± 1	—	—
Amorphous phases (volcanic glass, opal-A)	14 ± 5	66 ± 6	90 ± 3	68 ± 4	92 ± 2	37 ± 5	44 ± 5	59 ± 5	52 ± 5	—	72 ± 4
Kaolinite	—	—	—	2 ± 2	—	—	—	—	—	—	10 ± 2
Cristobalite	17 ± 4	1 ± 1	3 ± 1	1 ± 1	2 ± 1	4 ± 1	1 ± 1	7 ± 1	7 ± 1	—	3 ± 2
Quartz	—	<1	<1	<1	1 ± 1	1 ± 1	—	—	—	—	1 ± 0
Pyroxene	10 ± 2	—	—	—	—	22 ± 4	4 ± 3	9 ± 2	20 ± 4	—	3 ± 1
Plagioclase	37 ± 3	—	—	—	—	10 ± 3	5 ± 3	15 ± 2	18 ± 3	—	8 ± 3
Hematite	1 ± 1	—	—	—	1 ± 1	—	—	—	—	—	1 ± 0
K-Feldspar	14 ± 2	—	—	—	—	—	—	—	—	—	—

reasonably reliable in the range 10^{-12} to 10^{-15} m^2 (Farquharson et al., 2015). However, we note that some of our bedded ash tuff blocks were rectangular prisms (~50–60 mm in thickness); as a result, permeability estimates on these blocks were likely overestimated by the TinyPerm due to the volume of rock required for near-surface measurements of permeability (Selvadurai and Selvadurai, 2010). Estimates of permeability using the TinyPerm unit are not necessarily reliable for small ($\ll 100$ mm) samples. Some of the blocks collected appeared to have low-permeability skins; when present, we tried to remove the skin with a file prior to measurement. The permeability of each block was estimated using the mean of 3–4 TinyPerm II values measured at different locations on the surface of the block.

The bulk density of each of the 115 hand-sized sample blocks was estimated using the Archimedean weighing technique similar to that employed by Kueppers et al. (2005) and Farquharson et al. (2015). The dry weight W_d of each block was first measured using a balance (precision 0.1 g). The apparent immersed weight W_i was then measured by lowering each block into a water-filled bag suspended underneath a balance mounted on a tripod. The immersed weight was taken quickly to avoid water imbibition. The dry bulk density ρ_b of each block could then be determined using the following relation (assuming that the density of water = 1000 kg/m^3):

$$\rho_b = \frac{W_d}{W_d - W_i} \quad (1)$$

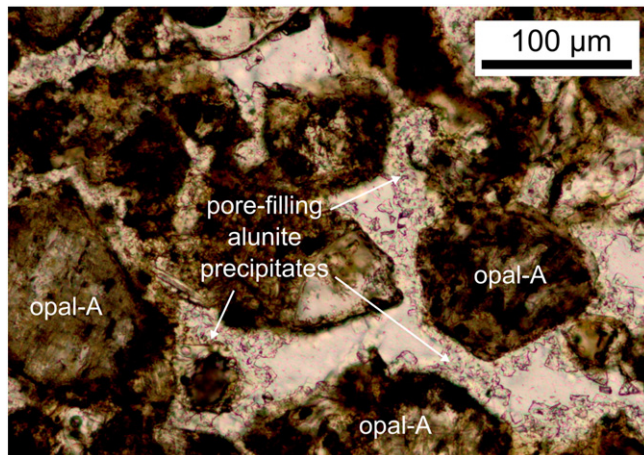


Fig. 5. Optical microscope image showing pore-filling alunite precipitates in a sample of ash tuff (WI21). Image taken from Heap et al. (2015a).

Four of the samples (WI-F-16, 46, 59, and 77; Supplementary Table S2) floated and we could not therefore determine their dry bulk density.

These dry bulk density values were converted to values of total porosity by measuring the solid density of each block. Once back in the laboratory, the blocks were cored to provide 20 mm-diameter cylindrical samples for laboratory measurements of porosity and permeability (see next section). The remainder of each block was powdered using a pestle and mortar. The solid density ρ_s (the density of each powder) was then measured using a helium pycnometer (Micromeritics AccuPyc II 1340). Total porosity was determined for each block using the following relation:

$$\phi_t = 1 - \left(\frac{\rho_b}{\rho_s} \right) \quad (2)$$

The total porosity of the four samples that floated (WI-F-16, 46, 59, and 77; Supplementary Table S2) was estimated by assuming a bulk dry density of 1000 kg/m^3 .

4.2.2. Laboratory methods

While field methods provide quick estimates for values of permeability and dry bulk density, such methods should always be groundtruthed by well-constrained measurements in the laboratory. Cylindrical samples (20 mm in diameter) were cored from the 115 hand-sized sample blocks and were precision ground so that their end faces were flat and parallel (Supplementary Figs. S6–S12). Samples were cored perpendicular to bedding, where present. The length of each core, which varied from ~22 to ~40 mm, was a function of the size and shape of the block. The length to width ratio of our samples was therefore greater than one in each case (length to width ratios lower than one are not recommended for laboratory permeability measurements). The samples were washed using water and then dried at 40°C in a vacuum oven for at least two days. The connected porosity of each core sample was measured using a helium pycnometer (Micromeritics AccuPyc II 1340). The samples were then jacketed (in a rubber jacket) and their permeability measured using a benchtop steady-state permeameter (see Farquharson et al., 2016; Heap and Kennedy, 2016) under a confining pressure of 1 MPa and at ambient laboratory temperature. A confining pressure during routine measurements of permeability is required to prevent gas travelling between the sample and the jacket. Samples were first left for one hour at a confining pressure of 1 MPa to ensure microstructural equilibrium. Flow rate measurements were taken (using either a low- or high-flow gas flowmeter, depending on the permeability of the sample) under several pressure gradients (typically from 0.05 to 0.2 MPa, equating to flow rates between 0.2 and 400 ml/min) to determine the permeability using Darcy's law and to assess the need for the Forchheimer and/or

the Klinkenberg corrections, which were applied on a case-by-case basis. The Klinkenberg correction corrects for gas slippage (Klinkenberg, 1941), and was typically applied to low-porosity, low-permeability samples with a high microcrack density. The Forchheimer correction (Whitaker, 1996) corrects for flow inertia and was typically employed for high-permeability samples that had to be measured using high flow rates.

Cylindrical samples (20 mm in diameter) were also taken from the nine larger blocks (WI20–26 and WI29–30) and precision ground to a nominal length of 40 mm (Figs. 4 and Supplementary Figs. S6–S12). Samples of the lava (WI20) were cored so as to contain none or one macroscopic (i.e., sample size) fracture along their axis (Fig. 4a). Samples of ash tuff WI21 were prepared to contain (1) no gas elutriation pipes (Fig. 4b), (2) gas elutriation pipes parallel to the sample axis (Fig. 4c) and, (3) gas elutriation pipes perpendicular to the sample axis (Fig. 4d). Samples WI22 and WI23 were cored perpendicular to the bedding direction (Fig. 4e and f). The porosity and permeability of these samples were measured using the same techniques described above (data are available in Supplementary Tables S4–S6). Further, to understand the influence of confining pressure (i.e., depth) on permeability, we performed experiments in which we sequentially measured the permeability of a sample of lava (WI20) and ash tuff (WI21) under confining pressures of 1, 2, 5, 10, 15, 20, 25, and 30 MPa (data available in Supplementary Table S7).

To explore their microstructure further, mercury injection tests were performed on pieces (2–5 g) of lava (WI20) and ash tuff (WI21–24) using the Micromeritics Autopore IV 9500 at the University of Aberdeen (Scotland). The evacuation pressure and evacuation time were 50 µm Hg and 5 min, respectively, and the mercury filling pressure and equilibration time were 0.52 pounds per square inch absolute (psia) and 10 s, respectively. The pressure range was 0.1 to 60,000 psia (i.e., up to a pressure of about 400 MPa). Mercury injection data permit the calculation of the pore throat size distribution within a particular sample.

5. Materials and methods for the unlithified materials

5.1. Field materials and methods for the unlithified materials

Eight localities within the recent, unlithified deposits of the crater floor at Whakaari were chosen for porosity and permeability analysis: four close to the crater lake (sites SP01, SP02, SP04, and SP07), two in a large gully on the north-eastern wall of the volcanic amphitheatre (sites SP06 and SP08), one near Troup Head (site SP05), and one near Crater Bay (SP03) (localities shown in Fig. 6). At each location, shovels were used to expose up to a couple of metres of fresh, vertical stratigraphy. Three of the near-crater localities (SP01, SP02, and SP04) exposed a similar stratigraphy (Fig. 6). The base of these deposits, only exposed at trench SP02, consists of a yellow-coloured ash/lapilli layer that contains a high percentage of large (~50 mm) lapilli fragments overlain by a similarly coarse black-coloured horizon of ash/lapilli. Above this coarse basal layer is a series of interbedded red- and grey/black-coloured deposits that likely represent cyclic phreatic to phreatomagmatic eruptions. These layers contain a noticeably smaller average particle size than the coarse basal layer. We interpret red- and yellow-coloured layers to be more hydrothermally altered than those black in colour. The deposits of the 2013 phreatic eruption mark the top of these crater floor deposits. The final near-crater trench (SP07) is located in a gully (several metres deep) draining southeast from Donald Duck crater. The flanks of this gully show signs of outgassing activity and the deposits are hydrothermally altered as a result. The deposits at this locality are yellow-grey in colour and contain few large lapilli fragments. The two sites chosen on the north-eastern wall of the volcanic amphitheatre (SP06 and SP08) were selected due to their differences in alteration. Further, these sites are both located within the 2004 landslide deposit that has an anonymously low gas flux (Bloomberg et al., 2014). Site SP06 contains a hydrothermally altered grey/yellow-coloured ash/

lapilli debris flow deposit that contains large (~50 mm) angular lapilli fragments below a laminated black/grey-coloured ash/lapilli deposit. Site SP08 comprises a grey-coloured ash/lapilli debris flow deposit that contains large (~50 mm) angular lapilli fragments. To measure characteristic reworked fluvial deposits not affected by hydrothermal alteration, we selected two sites located far from the crater lake and the volcanic amphitheatre rim (SP03 and SP05). Site SP03 contains a grey-coloured ash/lapilli deposit that is overlain by a similar deposit that contains large (~50 mm) angular lapilli fragments. Site SP05 consists of a brown-coloured ash/lapilli deposit.

A PL-300 soil permeameter (Umwelt-Geräte-Technik) was used to measure the permeability of the layers of unlithified material (for more information see Mayer et al., 2016b). Samples were first taken from the exposed stratigraphy using stainless steel cylinders (diameter 72 mm and length 61 mm; see inset in Fig. 6). The permeability could then be obtained using Darcy's law by measuring the volumetric flow rate of air through the sample. An internal vacuum pump produces the inflow of air through the sample, which is defined over a calibrated throat in the apparatus. The pressure difference over the sample is recorded by a sensor, which provides the pressure gradient of that flow. Comparison of the pressure gradient, with respect to a second gradient over the calibrated permeability of the internal throat, enables the determination of the volumetric flow rate of air through the sample and consequently the estimation of its permeability. The permeability of at least two samples from each distinguishable layer was measured (Supplementary Table S3). We also measured the temperature of each sample. The samples were then weighed and wrapped for transport.

Once back in the laboratory, the samples were oven-dried and their dry weight measured. The dry bulk density ρ_b could then be determined using the dry weight and the volume of the stainless steel cylinder. The solid density ρ_s (the density of the powder) was then measured using a helium pycnometer (Ultrapyc 1200e Quantachrome) and the total porosity determined using Eq. (2). Finally, the water content of each sample was calculated using the in-situ and the oven-dry weights.

5.2. Laboratory materials and methods for the unlithified materials

Two unlithified samples were collected for permeability measurement in the laboratory. The first was a poorly sorted unlithified tephra deposit, the most abundant material of the crater fill (Figs. 2 and 3g). The sample (WI27; Fig. 4i) was collected at a depth of one metre at the locality indicated in Fig. 1. The sample was first oven-dried. A portion of the sample was then poured into the rubber jacket and permeability was measured using the above-described procedure. Due to the size of our rubber jackets (inner diameter of 20 mm), large lapilli were first removed. The ash/lapilli sample (WI27; Fig. 4i) comprises mainly amorphous silica (59 wt.%), plagioclase (15 wt.%), pyroxene (9 wt.%), alunite (8 wt.%), and cristobalite (7 wt%) (Table 1). The porosity was measured by determining the dry bulk density of the sample within the jacket and the solid density (using the helium pycnometer); the total porosity could then be calculated using Eq. (2). The unlithified ash deposit sampled (WI28; Fig. 4j) formed part of the blanket of fine ash that covers large parts of the crater floor near the crater lake (Figs. 2 and 3h-i). The fine ash sample (WI27; Fig. 4i), collected from Donald Duck crater (see Fig. 1 for the collection locality), comprises mainly amorphous silica (52 wt.%), pyroxene (20 wt.%), plagioclase (18 wt.%), cristobalite (7 wt.%), and gypsum (3 wt%) (Table 1). In order to measure the in-situ permeability, we carefully wrapped the sample upon collection to preserve the in-situ water content (which was calculated to be ~0.25 by measuring the in-situ weight and oven-dry weight of a portion of the deposit). Once back in the laboratory, cylindrical samples (20 mm in diameter and nominally 40 mm in length) were taken by pushing a cylindrical metal sleeve into the sample. These cylindrical samples were then quickly and carefully jacketed (using a rubber jacket) and loaded into the permeameter. Due to the low permeability of the ash sample, the pressure decay method (Brace et al., 1968)

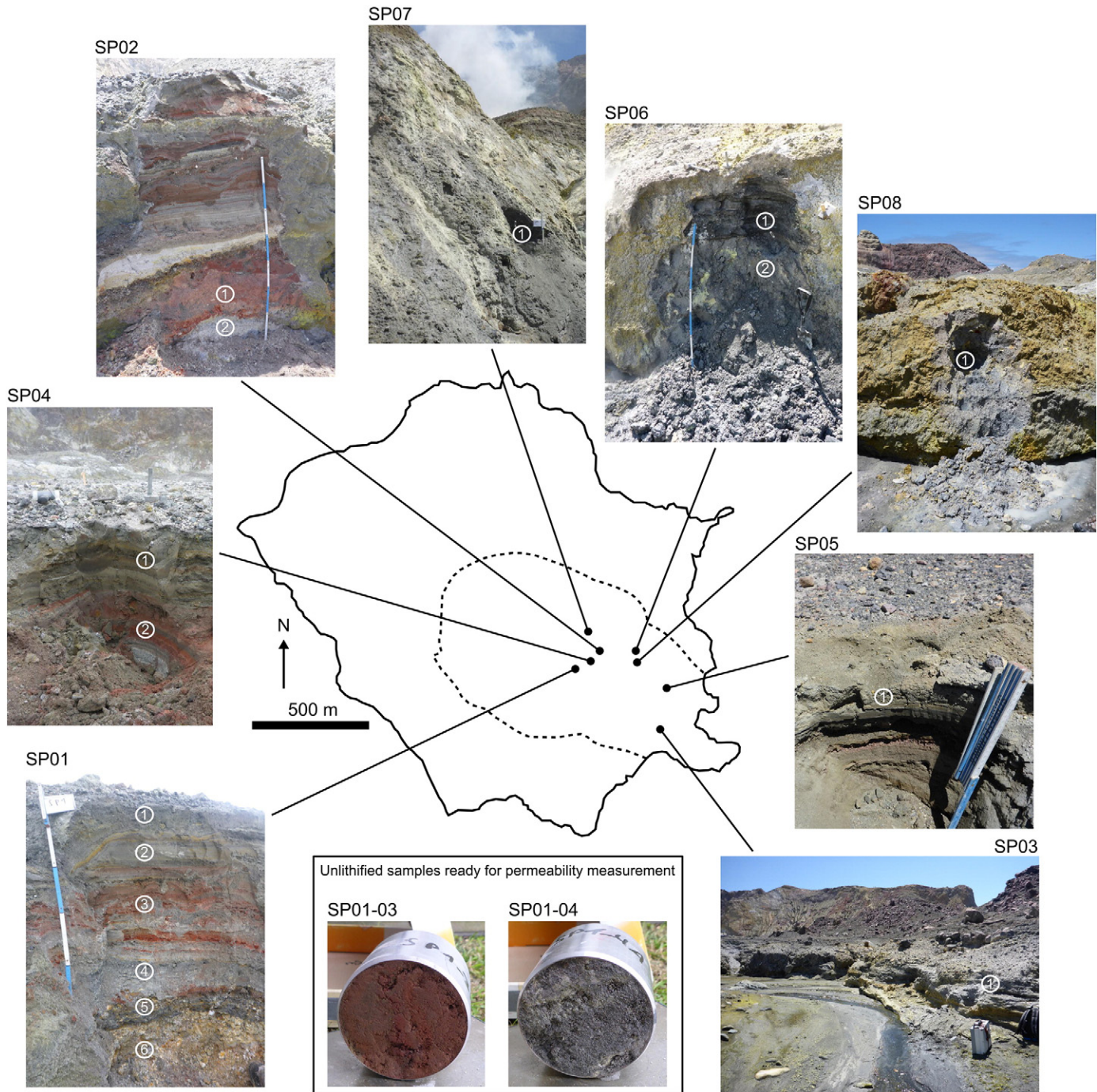


Fig. 6. Locality and photographs of each of the eight trenches dug for un lithified material analysis (permeability, porosity, water content, and temperature). Numbers on the pictures indicate the sample number (Supplementary Table S3). Inset shows two examples taken from trench SP01.

was used to determine their permeability. To do this, an initial increase (0.5 MPa) of the upstream pressure was applied to the sample and the fluid inlet closed. The permeability was then derived using the temporal decay of the upstream pressure. Owing to the delicate nature of WI27 and WI28, permeability measurements were conducted at confining pressures of 0.3 and 0.5 MPa, respectively.

6. Results

6.1. Field porosity and permeability of the lithified materials

Permeability as a function of dry bulk density for the 115 hand-sized sample blocks is shown in Fig. 7a (Supplementary Tables S1 and S2). We

find that the dry bulk density and permeability of the samples varies between 1000 and 2000 kg/m³ and between $\sim 10^{-15}$ and $\sim 10^{-11}$ m², respectively (Fig. 7a). When dry bulk density is converted to total porosity we find values between ~0.1 and ~0.6 (Fig. 7b). We find no discernible trends in the bulk density-permeability (Fig. 7a) or porosity-permeability (Fig. 7b) data, although we note that the lava and lava breccia samples (black circles) are typically denser/less porous than the ash tuffs (white circles) (Fig. 7).

6.2. Field porosity and permeability of the un lithified materials

The calculated total porosity of the un lithified deposits is plotted as a function of their stratigraphic depth in Fig. 8a. We find that porosity ranges

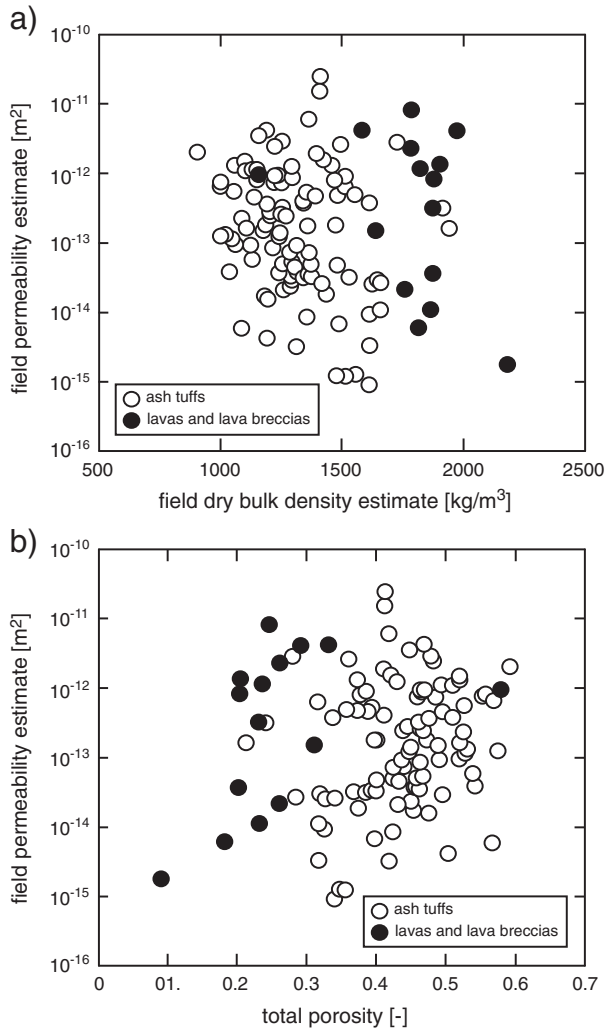


Fig. 7. Field measurements on the lithified hand-sized sample blocks collected. (a) Field permeability (using the TinyPerm II) as a function of field dry bulk density. (b) Field permeability (using the TinyPerm II) as a function of total porosity. Data are available in Supplementary Tables S1 and S2.

from ~ 0.25 to ~ 0.75 . There is no strong correlation between total porosity and the depth of the deposit (up to a maximum depth of ~ 140 cm; Fig. 8a). There is, however, a strong correlation between water content (calculated using the in-situ and dry weight of the sample) and depth (Fig. 8b): water content increases linearly with depth. As a result, the air-filled porosity in the deposits decreases as depth increases (Fig. 8c). Based on these data (Supplementary Table S3), the water table within the crater-fill deposits at Whakaari is at a depth of about 130–140 cm. We also note that the temperature of the deposit increases with increasing depth, from ~ 22 °C at the surface to ~ 50 –70 °C at a depth of ~ 100 cm (see inset in Fig. 8c). The data of Fig. 8 are available in Supplementary Table S3.

Since the gas moving through the sample can only travel through the air-filled porosity on the timescale of the measurement, we have chosen to plot permeability as a function of air-filled porosity (Fig. 9a). We see that, generally, permeability increases with increasing air-filled porosity. As a result, and although there is a lot of scatter, permeability is seen to decrease with depth (Fig. 9b). The data of Fig. 9 are available in Supplementary Table S3.

6.3. Laboratory porosity and permeability of the lithified materials

Permeability as a function of connected porosity for the 136 20 mm-diameter samples is shown in Fig. 10 (Supplementary Tables S4–S6).

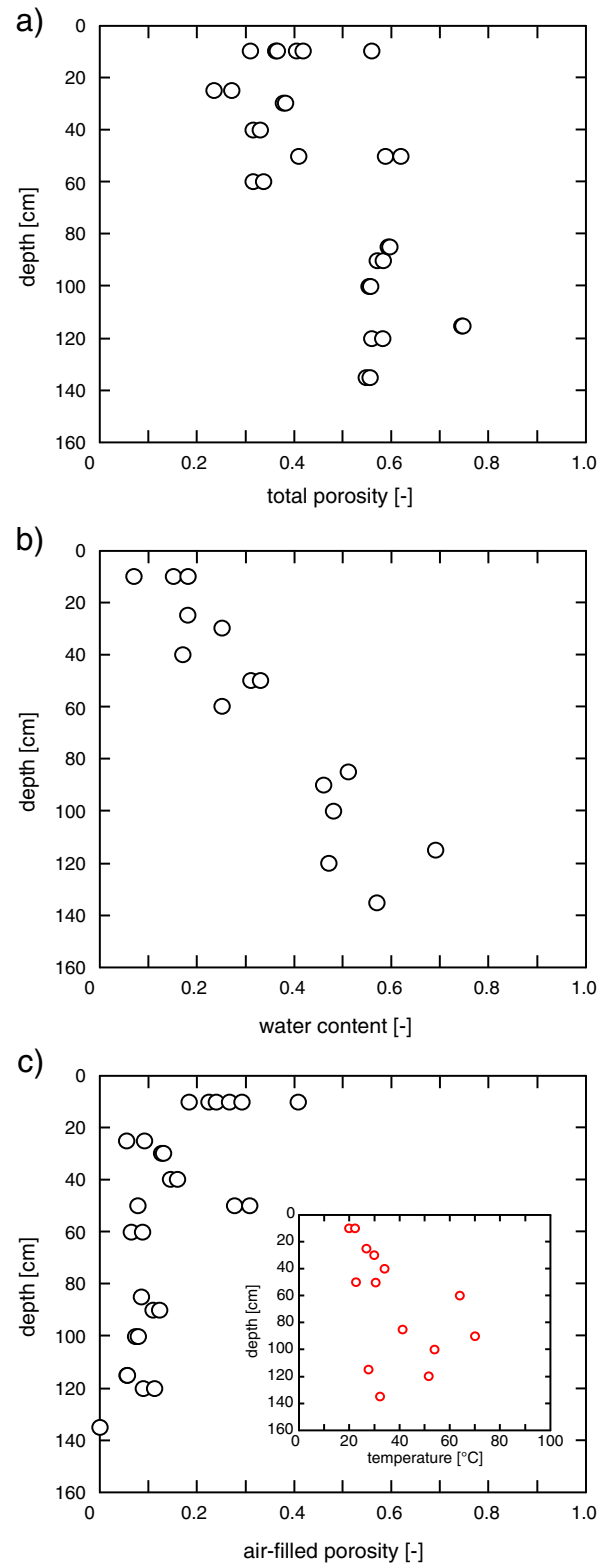


Fig. 8. Field measurements on the un lithified materials from the eight trenches shown in Fig. 6. (a) Depth as a function of total porosity. (b) Depth as a function of water content. (c) Depth as a function of air-filled porosity. Inset shows a graph of depth as a function of deposit temperature. Data are available in Supplementary Table S3.

We find that the connected porosity and permeability of the samples varies between ~ 0.1 and ~ 0.7 and between $\sim 10^{-15}$ and $\sim 10^{-11} \text{ m}^2$, respectively (Fig. 10). If one considers the lava and lava breccias and the ash tuffs separately, we find that, for both rock types, permeability

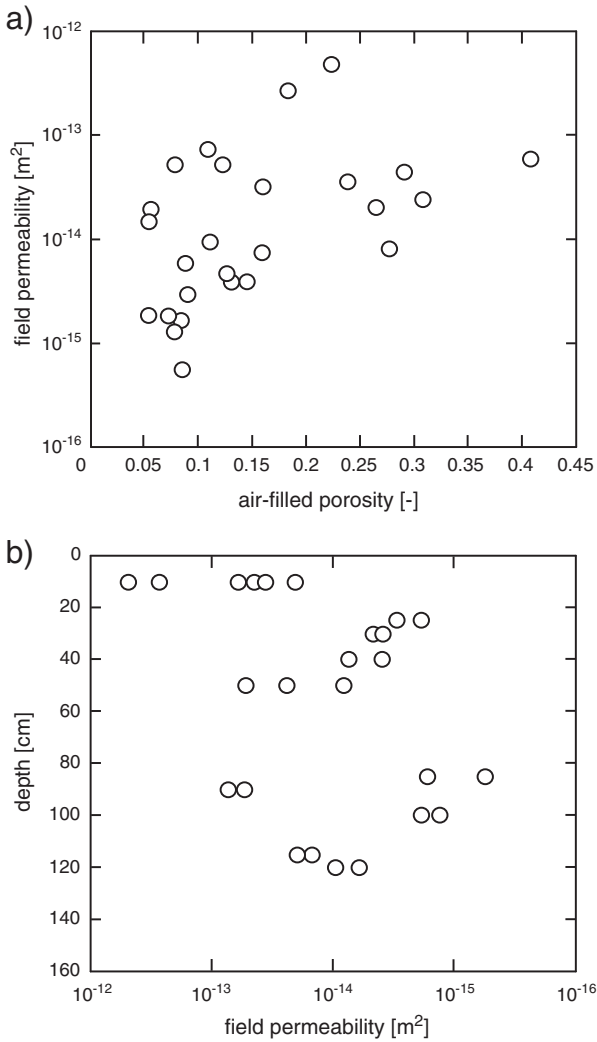


Fig. 9. Field measurements on the unlithified materials from the eight trenches shown in Fig. 6. (a) Field permeability as a function of air-filled porosity. (b) Depth as a function of field permeability. Data are available in Supplementary Table S3.

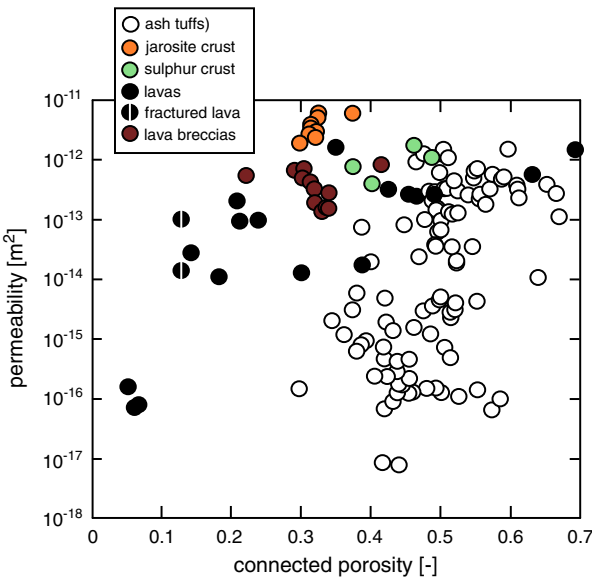


Fig. 10. Laboratory measurements of permeability as a function of connected porosity for all of the 20 mm-diameter cylindrical samples of this study, plotted on log-linear axes. Data are available in Supplementary Tables S4, S5, and S6.

increases as porosity increases (Fig. 10). In detail, increases in lava permeability are large as connected porosity is increased when the porosity is low (less than ~0.15) and small as connected porosity is increased when the porosity is high (greater than ~0.15) (Fig. 10). All of the lava breccia samples contain a porosity >0.2 and therefore form part of the latter trend. We also note that the jarosite (orange circles) and sulphur (green circles) crusts do not plot within the broad porosity-permeability trend defined by the ash tuff samples: the jarosite crust samples in particular were considerably more permeable than ash tuffs of a similar porosity (Fig. 10; Supplementary Table S6). The permeability of the prepared sulphur flow samples was too low for measurement in our bench-top permeameter (permeability < 10⁻¹⁸ m²) (Supplementary Table S6).

6.3.1. Influence of macrocracks on the permeability of lava

The presence of a macrocrack (parallel to the direction of flow) in samples of lava serves to greatly increase their porosity and permeability (Supplementary Table S4). Porosity increased from 0.036 to between 0.092 and 0.112 when a macrocrack was present. Permeability increased from 1.6×10^{-16} m² (macrocrack-free sample) to 1.4×10^{-14} and 1.1×10^{-13} m² for the macrocracked samples containing porosities of 0.092 and 0.112, respectively (Supplementary Table S4). We use here the two-dimensional model proposed by Heap and Kennedy (2016) to determine their fracture permeabilities k_f :

$$k_f = \frac{A k_e A_{intact} \cdot k_0}{A_{fracture}} \quad (3)$$

Where A , $A_{fracture}$, and A_{intact} are the areas of the sample end face, the fracture, and the intact portion of the sample end face, respectively, and k_e and k_0 are the equivalent (i.e., the permeability of the fractured sample) and intact permeabilities, respectively. Assuming a constant throughgoing fracture width of 0.5 mm, we calculate fracture permeabilities of 4.3×10^{-13} and 3.3×10^{-12} m² for the macrocracked samples containing porosities of 0.092 and 0.112, respectively (Supplementary Table S4).

6.3.2. Influence of gas elutriation pipes on the permeability of ash tuff

To assess the influence of gas elutriation pipes on the permeability of the ash tuffs, permeability was measured on samples of WI21b containing gas elutriation pipes orientated either parallel or perpendicular to the direction of fluid flow (Fig. 11; Supplementary Table S5). Although the sample with the highest permeability (3.1×10^{-15} m²) contains gas elutriation pipes parallel to flow, we note that two similarly prepared

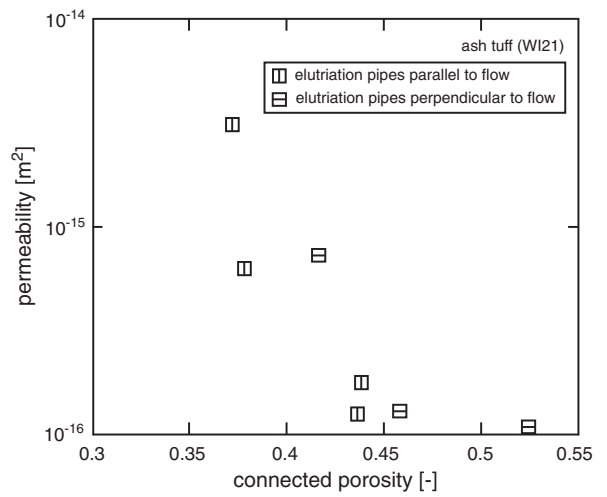


Fig. 11. The influence of gas elutriation pipes on the permeability of ash tuff (WI21). Graph is a plot of permeability (measured in the laboratory; data available in Supplementary Table S5) as a function of connected porosity.

samples have permeability values $\sim 10^{-16} \text{ m}^2$ (Fig. 11; Supplementary Table S5). It is difficult therefore to draw firm conclusions as to the influence of gas elutriation pipes on the permeability of the ash tuff from these data.

6.3.3. Influence of confining pressure on permeability

The influence of confining pressure (up to 30 MPa) on the permeability of a lava sample (WI20; without macrocracks) and an ash tuff sample (WI21b; parallel gas elutriation pipes) is presented in Fig. 12 (data available in Supplementary Table S7). Assuming a constant bulk density for WI20 and WI21 of 2500 and 1500 kg/m³, respectively, the depth at a pressure of 30 MPa was estimated using $P = \rho g z$ to be ~ 1.2 and ~ 2 km for WI20 and WI21, respectively. The reduction of permeability with increasing pressure is much higher for the lava than for the ash tuff sample (Fig. 12). The permeability of the ash tuff was reduced from $7.6 \times 10^{-15} \text{ m}^2$ at a confining pressure of 1 MPa down to $4.7 \times 10^{-16} \text{ m}^2$ at 30 MPa. In the same pressure range, the permeability of the lava deposit was reduced from $1.0 \times 10^{-16} \text{ m}^2$ to $2.4 \times 10^{-17} \text{ m}^2$. In both cases, the largest permeability decrease was seen as the confining pressure was increased from 1 to 2 MPa. Following this initial decrease, the permeability decreased more-or-less monotonously with increasing confining pressure (Fig. 12).

6.3.4. Pore throat diameter of lava and ash tuffs

The pore throat diameter distributions, as measured by mercury injection, for the lava sample (WI20) and the four ash tuffs (WI21, WI22, WI23, and WI24) are presented in Fig. 13. For the lava we find that only 5% of the pore throats have a diameter larger than 0.2 mm; the majority of the pore throats (95%) are between 0.2 and 0.004 mm in diameter. The most abundant pore throat diameter for WI20 is 0.006 mm. The pore throat diameter distributions for the ash tuffs are very different to that of the lava: the ash tuffs contain a much larger proportion of larger pore throats (Fig. 13). Indeed, pore throats $>100 \mu\text{m}$ were measured in the ash tuffs. The pore throat diameter distributions for the different ash tuffs are quite similar, although we note that WI24 contains a lower proportion of small ($< 0.04 \text{ mm}$) pore throats than the other ash tuffs. The most abundant pore throat diameters are 0.1, 0.006, 0.05, and 0.04 mm for WI21, WI22, WI23, and WI24, respectively (Fig. 13).

6.4. Laboratory porosity and permeability of the unlithified materials

The total porosity of the unlithified ash/lapilli (dried) and the fine ash (dried) were calculated to be 0.54 and 0.45, respectively. Since the in-situ water content of the fine ash is ~ 0.25 , the air-filled porosity of

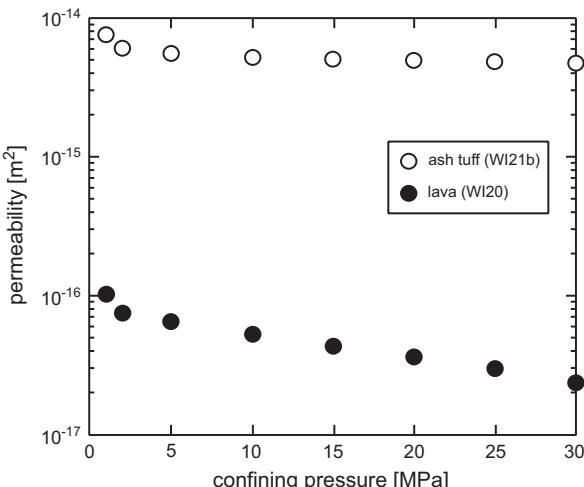


Fig. 12. The influence of confining pressure (depth) on the permeability of lava (WI20) and ash tuff (WI21). Graph is a plot of permeability (measured in the laboratory; Table 4) as a function of confining pressure. Data are available in Supplementary Table S7.

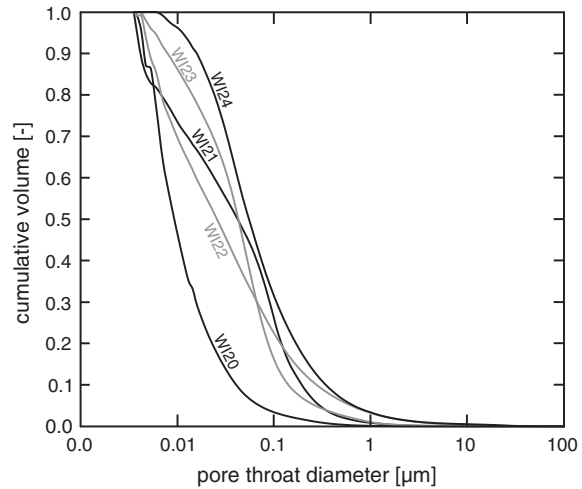


Fig. 13. The distribution of pore throat diameters for samples WI20 (lava), WI21, WI22, WI23, and WI24 (ash tuffs) determined through mercury injection tests.

the in-situ deposit is estimated to be ~ 0.2 . The permeability of the unlithified ash/lapilli (dried) and the fine ash (in-situ water content ~ 0.25 ; air-filled porosity ~ 0.2), as measured in the laboratory, were 3.36×10^{-12} and $4.50 \times 10^{-19} \text{ m}^2$, respectively.

7. Discussion

7.1. Laboratory versus field measurements

The total porosity and permeability determined in the field is compared with laboratory measurements on the samples cored from the same block in Fig. 14. We find that laboratory porosity is typically slightly higher than the porosity measured in the field, but that there is no systematic variation with increasing porosity (Fig. 14a). It is likely that dry bulk density is overestimated using the field technique due to the imbibition of water, an offset that could be corrected empirically (Farquharson et al., 2015). However, estimates of permeability using the TinyPerm II unit over- or underestimated the permeability of the measured rocks by two or in some cases three orders of magnitude (Fig. 14b). For the most part, the permeability measured by the TinyPerm II unit overestimated the permeability; this is perhaps due to the fact that the permeability of some blocks was too low to be measured by the TinyPerm II (although the unit gives a value regardless). Overestimates could also be due to an imperfect seal between the rock and the nozzle due to an uneven rock surface and/or due to the presence of a low-permeability skin (although, as noted above, we tried to remove low-permeability skins prior to measurement). It is clear from these data that, although the TinyPerm II unit offers a quick and easy estimate of permeability, such estimates should be groundtruthed by well-constrained laboratory data.

7.2. Porosity and permeability relationships in the lithified materials

Generally speaking, the permeability of porous media increases with increasing connected porosity (e.g., Bourbié and Zinszner, 1985; Wadsworth et al., 2016). However, the link between porosity and permeability is not straightforward, as permeability does not strictly rely on porosity, but on the connectivity and geometry of the porosity (crack porosity versus pore porosity, pore and crack geometries, pore and crack tortuosity, amongst other factors). In other words, low-porosity rocks can have a high permeability, and vice versa. Volcanic rocks in particular display a wide range of microstructure and laboratory studies have exposed porosity-permeability relationships for a variety of volcanic rocks (Klug and Cashman, 1996; Saar and Manga, 1999; Rust and Cashman, 2004; Mueller et al., 2005; Wright et al., 2009; Farquharson

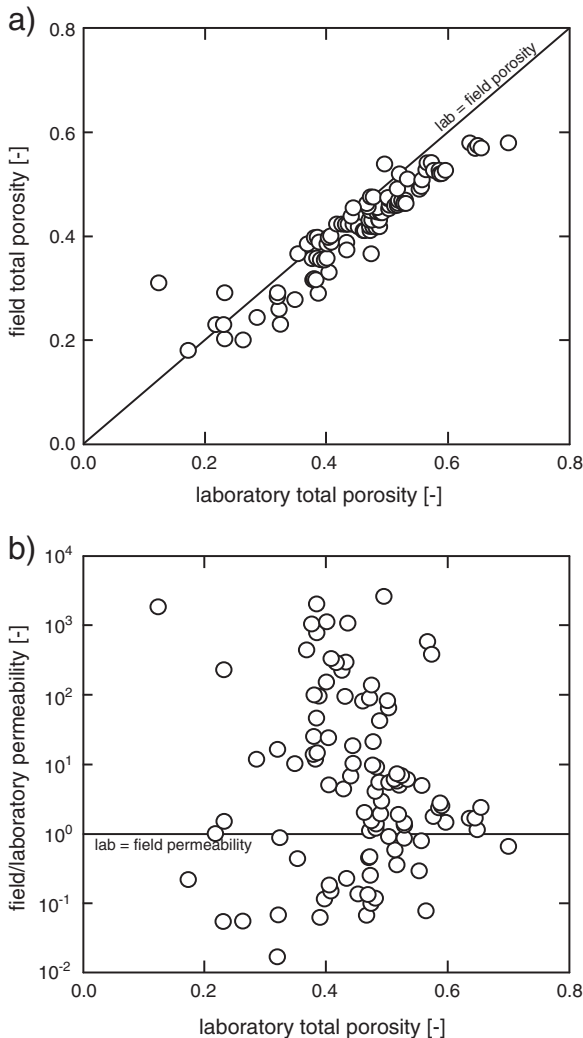


Fig. 14. Laboratory versus field measurements of porosity and permeability. (a) Field total porosity as a function of laboratory total porosity. (b) The ratio of field to laboratory permeability as a function of laboratory total porosity.

et al., 2015; Kennedy et al., 2016; Kushnir et al., 2016; Heap and Kennedy, 2016). Few laboratory studies however have measured the porosity and permeability of hydrothermally altered volcanic rocks (e.g., Siratovich et al., 2014; Mayer et al., 2016a, 2016b). Our study has shown that the porosity-permeability relationships for the hydrothermally altered materials that form Whakaari are complex (Fig. 10). Due to the limitations of TinyPerm II field permeameter (Fig. 14b), in the following discussion we will focus solely on laboratory measurements of porosity and permeability (Fig. 10).

We also highlight that the measurements of porosity and permeability provided herein were determined using gas (helium and nitrogen, respectively). It is well known that measurements of permeability will be influenced by the presence of clays (Faulkner and Rutter, 2000; Tanikawa and Shimamoto, 2009), which is the case for two of the samples collected (WI23 and WI30; Table 1). The measurements of permeability provided here will therefore overestimate the permeability of these samples to water, since water will serve to swell the clays present within the rock and hence reduce the permeability. However, it is unclear at present the influence of hydrothermal brines and seawater on the permeability of clay-bearing rocks.

It is also important to note that laboratory measurements of permeability are scale-dependent (Brace, 1984; Clauer, 1992; Neuman, 1994; Heap and Kennedy, 2016; Farquharson et al., 2016). Due to the small size of laboratory samples, measurements of permeability in the

laboratory do not account for macroscopic features (such as macroscopic fractures or bedding). They will therefore under- or overestimate the equivalent permeability if the macroscopic feature provides a pathway or a barrier to fluid flow, respectively.

7.2.1. Porosity and permeability relationships in the lavas and lava breccias

We find that a single power law cannot describe the porosity-permeability trend for the lavas and lava breccias (Fig. 10). While porosity-permeability relationships for volcanic rocks have been classically described using a single power law model (e.g., Mueller et al., 2005), recent studies have invoked a double power law model (Farquharson et al., 2015; Heap et al., 2015b; Kushnir et al., 2016; Heap and Kennedy, 2016). The double power law model consists of two discrete power laws that intersect at a so-called “porosity changepoint” x^* . The use of two power laws in these studies, as opposed to one, has been statistically verified using Bayesian Information Criterion (BIC) analysis (e.g., Main et al., 1999). The physical meaning of the porosity changepoint is thought to represent a change in microstructure. Low-porosity volcanic rocks often contain a poorly connected or tortuous network of pores, and fluids are often obliged to travel through narrow microcracks that connect the pore network (Heap et al., 2014; Farquharson et al., 2015; Kushnir et al., 2016; Heap and Kennedy, 2016). Moderate- to high-porosity volcanic rocks, by contrast, often contain a well-connected network of large pores and channels (Rust and Cashman, 2004; Wright et al., 2006; Farquharson et al., 2015; Kennedy et al., 2016; Kushnir et al., 2016; Heap and Kennedy, 2016). The porosity changepoint in these studies lies within a narrow range of porosity: between 0.15 and 0.2 (Farquharson et al., 2015; Heap et al., 2015b; Kushnir et al., 2016; Heap and Kennedy, 2016). Applying the same BIC analysis to the lava and lava breccia data of this study confirms that they are statistically better described by two power laws that intersect at a changepoint porosity of ~ 0.14 (Fig. 15), rather than a single power law. The determined changepoint is similar to those found for extrusive andesites and basaltic-andesites (Farquharson et al., 2015; Kushnir et al., 2016; Heap and Kennedy, 2016) and viscously densifying block-and-ash flow deposits (Heap et al., 2015b). The physical meaning of the porosity changepoint in the lavas and lava breccias from Whakaari appears consistent with that described by these previous studies. Lava sample WI20—which contains a porosity of ~ 0.06 (i.e., below the changepoint)—contains

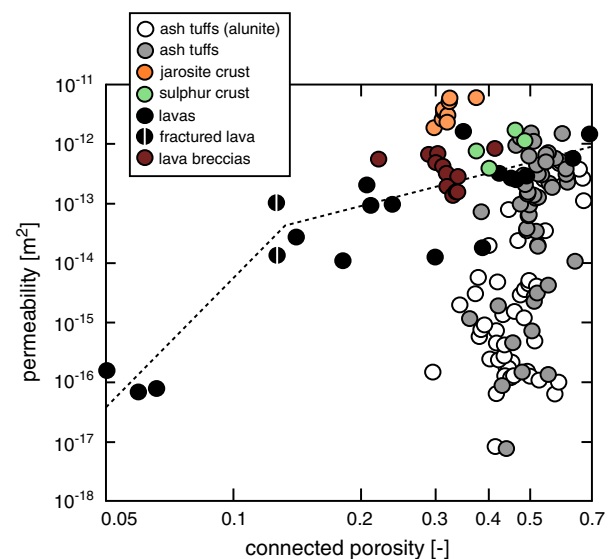


Fig. 15. Laboratory measurements of permeability as a function of connected porosity for all of the 20 mm-diameter cylindrical samples of this study, plotted on log-log axes. The dashed lines indicate the two best-fit power law curves through the data, as determined using modified Bayesian Information Criterion (BIC) analysis (see text for details). Data are available in Supplementary Tables S4, S5, and S6.

few pores that are connected by a tortuous network of microcracks (Fig. 4a). Indeed, mercury injection analysis shows that the majority of the pore throats (95%) are between 0.2 and 0.004 mm in diameter (i.e., microcracks connect the porosity; Fig. 13) and the application of modest confining pressures significantly reduced the permeability, interpreted as a consequence of the closure of compliant microcracks (Fig. 12; see also Vinciguerra et al., 2005 and Nara et al., 2011). By contrast, sample WI-F-96 contains a very high porosity ~0.65 (i.e., above the changepoint) and contains a network of presumably well-connected channels that are visible with the naked eye (Supplementary Figs. S1 and S6).

We find that, despite the hydrothermal alteration of the lavas (Figs. 4a, 4l, and Supplementary Fig. S6), their values of porosity and permeability are not dissimilar to those for unaltered lavas (e.g., Farquharson et al., 2015; Kushnir et al., 2016; Heap and Kennedy, 2016). However, we stress that alteration must greatly modify the porosity structure of a material to greatly modify porosity and permeability. This is typically not the case for the studied altered lava samples (Figs. 4a, 4l, and Supplementary Fig. S6). For example, we find that pore- and fracture-filling precipitation is rare in the lavas collected (Supplementary Figs. S6–S7): a modest volume of cristobalite (14 wt.%) and minor jarosite and gypsum precipitation is present in sample WI20 (although the presence of pore-filling cristobalite may not decrease permeability if associated with microporous diktytaxitic textures; Kushnir et al., 2016) and kaolinite (10 wt.%) is present in sample WI30 (although it is not clear whether such clays are associated with mineral replacement or pore- or crack-filling precipitation). Indeed, lava sample WI20 can be classified only as moderately altered, since less than half of the original mineral phases have been altered or replaced (BS5930, 1999). We do note, however, that hydrothermal alteration of the lava likely contributed to the growth of the macrocracks that are commonly found within the lavas at Whakaari (e.g., Fig. 4a); hydrothermal alteration has been previously shown to reduce material strength (Pola et al., 2012; Frolova et al., 2014; Wyering et al., 2014). We show here that such macrofractures can increase sample permeability by a three orders of magnitude (Supplementary Table S4; Fig. 15), in accordance with previous studies on the influence of macrofractures in volcanic rock (Nara et al., 2011; Heap and Kennedy, 2016). An example of such a fracture in the lavas at Whakaari is provided in Fig. 16a. A second noteworthy observation is that macrocracks within the lavas can be efficiently sealed with hydrothermal precipitates (see the example in Fig. 16b). Andesite blocks ejected from the 1978 crater also contained 5–10 mm wide veins of alunite, anhydrite, and Al-rich chlorite (Hedenquist et al., 1993). Progressive precipitation within fractures will greatly reduce their permeability (Edmonds et al., 2003; Griffiths et al., 2016).

The high permeability of the fractures within low-permeability lava ($\sim 10^{-13}$ to $\sim 10^{-12} \text{ m}^2$) coupled with the presence of fracture-filling precipitation suggests that such fractures are preferentially used as pathways for hydrothermal fluids. Therefore, high-permeability fractured (altered) lavas could be modified to low-permeability lavas containing sealed fractures over time, providing that the fluid temperature and composition (including pH) support mineral precipitation.

7.2.2. Porosity and permeability relationships in the tuffs and crusts

The porosity-permeability relationship for the ash tuffs is considerably more scattered than that for the lavas and lava breccias, although there is a general trend of decreasing permeability with decreasing porosity (Fig. 15). We highlight that the observation of a trend in these data is only made possible by the large number of datapoints ($n \sim 100$; Supplementary Tables S5–S6), a prerequisite for understanding relationships in rocks with variable microstructures due to variable alteration styles and intensities. We observe no porosity changepoint in the ash tuff data. The absence of two distinct porosity/permeability trends is likely due to the absence of two distinct microstructural groups in the ash tuff samples (i.e., microcracks and few pores versus

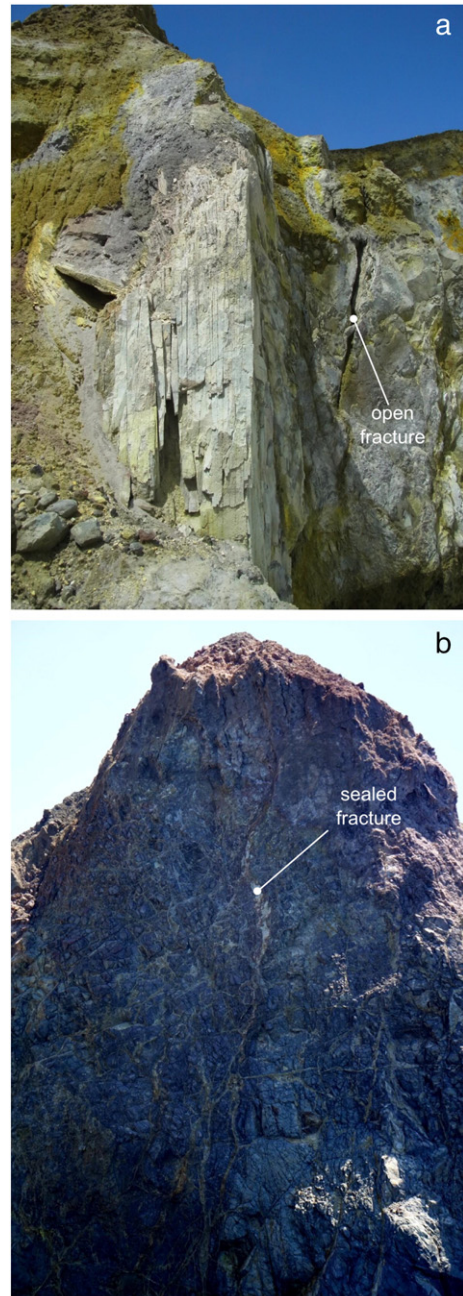


Fig. 16. Macroscopic fractures in lavas at Whakaari. (a) Open fractures near the crater rim that could act as pathways for the subvertical flow of hydrothermal fluids. (b) Examples of sealed fractures that could significantly reduce the permeability of the lava.

a well-connected pore network). If microcracks were present in all of the ash tuff samples, it would serve to increase the permeability of the low-permeability samples, but would not significantly change the permeability of the high-permeability samples (see also Heap and Kennedy, 2016), thus potentially creating a changepoint. Microcracks were not observed during our SEM analysis of the ash tuff samples (Fig. 4b–f) and mercury injection analysis showed that pore throats can be as large as ~100 µm (i.e., pores; Fig. 13). The modest decrease in permeability as confining pressure is increased is further evidence of the absence of microcracks in the ash tuff samples (Fig. 12). However, we highlight that a changepoint can exist for granular, microcrack-free materials (Bourbié and Zinszner, 1985; Heap et al., 2015b). It is possible therefore that a microstructural changepoint could exist for the ash tuffs of this study at a lower porosity (~0.1–0.15), in accordance with those found for sandstone (Bourbié and Zinszner, 1985) and welded

pyroclastic deposits (Heap et al., 2015b). This assertion is supported by the very low porosity and permeability of the highly cemented sulphur flow samples (WI29; Supplementary Table S6) which, if plotted on Fig. 15, would presumably not follow the single power law trend defined by the measured ash tuff samples. However, based on our data (Fig. 15), low-porosity and low-permeability ash tuffs at Whakaari are likely rare and potentially restricted to vent-proximal deposits cemented by sulphur.

Despite the trend of decreasing permeability with decreasing porosity, the permeability of the ash tuff can vary by up to five orders of magnitude for a single value of porosity (Fig. 15). This is due to the considerable microstructural variability between the samples (particle size, pore size, amongst others; Supplementary Figs. S8–S11). If we first consider alteration style, we find that white-coloured ash tuff samples (their white colour is indicative of alunite, a sulphate that is found as a replacement mineral and as a pore-filling precipitate; Fig. 5; Heap et al., 2015a; Mayer et al., 2015) are typically of lower porosity and permeability (white circles in Fig. 15) than grey-, brown-, and red/purple-coloured ash tuff samples (samples that do not contain alunite; grey circles in Fig. 15). It is possible that porosity and permeability were reduced in these samples due to the precipitation of pore-filling alunite, a consequence of their exposure to acid-sulphate fluids. Alunite precipitates from low-pH solutions (Browne, 1978; Ece et al., 2008), typically between 2.5 and 3.0 (Browne, 1978), and requires the formation of sulphuric acid either by (1) atmospheric oxidation of iron sulphides (supergene environment), (2) atmospheric oxidation near the water table of H₂S from deeper boiling fluids (steam-heated hydrothermal environment) and (3) disproportionation of SO₂ to H₂SO₄ and H₂S from a condensing magmatic vapour plume (magmatic hydrothermal environment) (Rye et al., 2002; Mutlu et al., 2005; Zimbelman et al., 2005; Ece et al., 2008; Pirajno, 2009). Therefore, progressive alunite precipitation could reduce porosity and permeability in accordance with the porosity-permeability trend shown in Fig. 15, although we note that tuffs without alunite alteration can also be of low porosity and permeability. While the observation that the density of rocks within the Biga Peninsula (Turkey) increases with alunite content (Ece et al., 2008) supports such a hypothesis, firm conclusions cannot be drawn without undertaking laboratory-controlled precipitation experiments.

We further note that some alunite-bearing samples contain very small pores (i.e., pores that cannot be seen with the naked eye; WI-F-3, WI-F-52, WI-F-110, and WI-F-112; Supplementary Figs. S8–S11) and that these samples all have very low permeabilities of $\sim 10^{-17}$ m² (Supplementary Table S5). It is likely that the pore radii in these samples have been dramatically reduced by pervasive alunite precipitation, explaining their low permeability (although a high density of very small pores allows the rock to maintain a high porosity). Such low-permeability layers can also exist as thin (~2–4 mm) layers (as is the case for WI-F-4; Supplementary Fig. S8). The thin layer in samples of WI-F-4, oriented perpendicular to the measurement of permeability, dramatically reduced sample permeability: the permeability of these samples is also $\sim 10^{-17}$ m² (Supplementary Table S5).

Therefore, shallow tuffs that exist within pathways for hydrothermal fluids may be of lower porosity and permeability than those shielded from acid-sulphate fluids, provided that the fluid temperature and composition (including pH) support mineral precipitation. Near active vents and fumaroles, where the pH may preclude alunite precipitation (pH can be close to unity; Gigganbach et al., 2003), the cementation of tephra deposits and tuffs by sulphur can effectively destroy porosity and permeability (as is the case for the sulphur flow sample WI29; Supplementary Table S6; see also Harris and Maciejewski, 2000; Christenson et al., 2016).

Macroscopic textures add another degree of complexity. We observe gas elutriation pipes (e.g., sample WI21; Supplementary Figs. S8–S11) and bedding (e.g., samples WI22 and WI23; Supplementary Figs. S8–S11) in some of the samples collected. Although the influence of bedding-perpendicular gas elutriation pipes on permeability is unclear with the available data (Fig. 11), we anticipate that the observed

bedding will promote a permeability anisotropy within the ash tuff deposits (not tested systematically here due to the limited size of the blocks collected), especially if adjacent interbedded layers or laminations have disparate values of porosity and permeability (e.g., WI-F-4; Supplementary Fig. S8). Bedding-induced permeability anisotropy will favour the lateral movement of fluids over the vertical movement of fluids.

The porosity and permeability of the crust (jarosite and sulphur) samples (Supplementary Fig. S12) is distinct from the ash tuffs (Fig. 15; Supplementary Tables S5–S6). The jarosite crust samples in particular are much more permeable (about 5 orders of magnitude) than ash tuffs of a similar porosity. In terms of porosity-permeability, the crust samples are similar to porous sandstones. For example, the permeability of Berea sandstone (porosity = 0.21) is about 5.0×10^{-12} m² (Zhu and Wong, 1997). The higher permeability of the crust samples and the ash tuff samples can be explained by their larger pore size compared to the ash tuffs (Fig. 4). The presence of larger pores is likely due to the fact that these surficial deposits are yet to undergo compaction as a result of burial by more recent tephra deposits.

7.3. Porosity and permeability relationships in the unlithified materials

The outgassing of magmatic volatiles and the movement of hydrothermal fluids through and within the shallow crater floor must rely on the permeability of the surficial, unlithified ash/lapilli deposits. When dry, the unlithified crater-fill deposits have a high permeability of $\sim 10^{-12}$ m² (measured in the laboratory). Under in-situ (i.e., partially-saturated) conditions, we measured permeabilities between $\sim 10^{-15}$ and $\sim 10^{-12}$ m² (Fig. 9; Supplementary Table S3) for the unlithified materials of the crater floor, values not dissimilar to the ash tuffs (Fig. 15). Samples at or very close to complete saturation (>1 m depth) had permeabilities too low to be measured by the PL-300 soil permeameter (Supplementary Table S3). We find that permeability decreases with the available air-filled porosity and with depth (Fig. 9). It is important to note that the in-situ values of field permeability for the unlithified deposits are relevant for gases (e.g., CO₂) moving through deposits partially saturated with aqueous fluids; these values likely, therefore, considerably underestimate the permeability of these deposits to aqueous solutions.

To understand the role of texture on the permeability of the unlithified deposits, we plot those deposits containing large lapilli fragments as squares whilst deposits without large lapilli fragments are plotted as circles (Fig. 17). We find that there is no correlation between the presence/absence of large lapilli and porosity-permeability (Fig. 17). We also use these data to assess the impact of alteration on the porosity and permeability values of these unlithified deposits. The red-coloured deposits—interpreted here as high alteration layers—are plotted as red symbols, the highly altered deposit at SP07 (Fig. 6) is plotted as a yellow symbol, and the largely unaltered deposits of trench SP05 and SP08 (Fig. 6) are shown as grey symbols in Fig. 17. In highlighting these data we see that there is no obvious correlation between alteration and porosity and permeability (Fig. 17). It follows that, since we see no evidence of compaction (Supplementary Table S3), permeability to gas in these deposits simply decreases with depth due to the increase in water saturation with depth (Figs. 8 and 9). To modify permeability of a material, the alteration must modify the structure of the porosity (e.g., through dissolution, precipitation, alteration-induced cracking). However, if the deposit remains unlithified, the alteration must have simply resulted in devitrification, oxidation, or mineral replacement of the ash and lapilli particles; there was therefore no change to the interstitial void space, and therefore no change to the porosity or permeability. However, permeability may be reduced if the alteration results in the formation of clay minerals. Therefore, despite the absence of a correlation between alteration and porosity/permeability in our data (Fig. 17), we do not preclude here alteration-induced changes to porosity/permeability in the unlithified deposits at Whakaari.

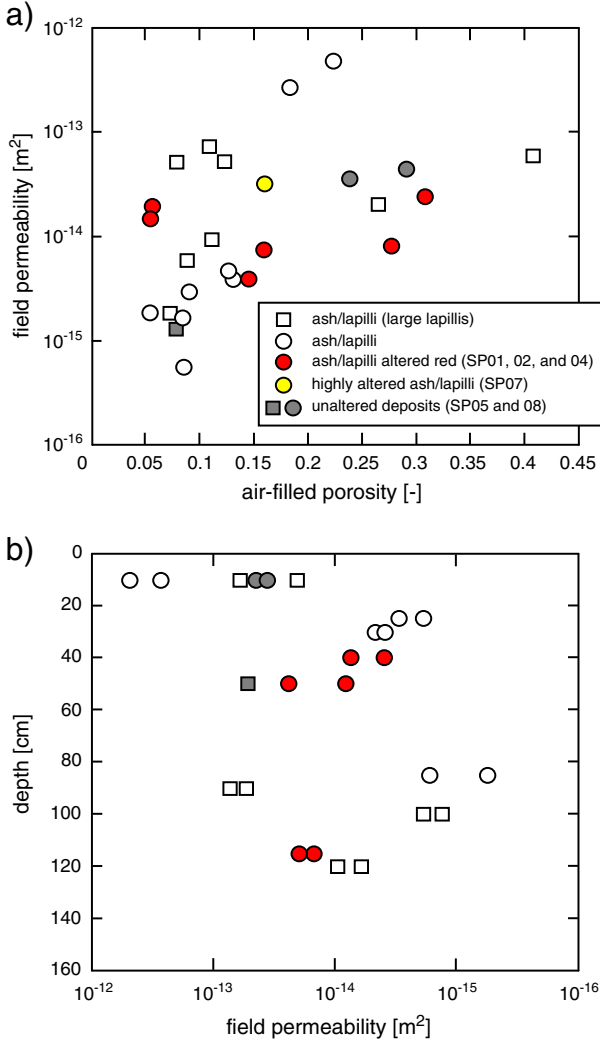


Fig. 17. Field measurements on the un lithified materials from the eight trenches shown in Fig. 6. (a) Field permeability as a function of air-filled porosity. (b) Depth as a function of field permeability. Graphs have been modified from Fig. 9 to show textural features (lapilli or no lapilli) and alteration intensity. Data are available in Supplementary Table S3.

Values of permeability between $\sim 10^{-15}$ m² and $\sim 10^{-12}$ m² were measured for the un lithified crater-fill deposits (Fig. 9; Supplementary Table S3). Therefore, the circulation and passage of fluids within and through the deposits of the crater floor should be largely unimpeded. However, gases may struggle to quickly negotiate through deeper deposits that are close to complete water saturation. Indeed, samples at or very close to complete saturation (>1 m depth) had permeabilities too low to be measured by the PL-300 soil permeameter (Supplementary Table S3). The movement of fluid (both gases and aqueous solutions) will be strongly inhibited by the layers of partially saturated fine ash however (such as that near Donald Duck and Noisy Nellie craters; Fig. 3h-i), which has an in-situ permeability of $\sim 10^{-19}$ m² (measured in the laboratory). Blankets of fine ash within the un lithified crater floor deposits will create a permeability anisotropy and are likely to strongly inhibit the vertical movement of hydrothermal fluids.

8. Conclusions and implications for Whakaari (White Island volcano)

Understanding the eruptive behaviour of, and modelling unrest at, Whakaari rests on a detailed comprehension of the permeability of the materials that form and exist within the crater. We find that the assembled products at Whakaari vary considerably in terms of porosity

and permeability: porosity ranges from ~ 0.01 up to ~ 0.7 and permeability spans eight orders of magnitude (from $\sim 10^{-19}$ to $\sim 10^{-11}$ m²). This variability is due to the variable rock types forming the flanks of the volcano and filling the craters (tuffs, lavas, lava breccias, and un lithified tephra), their varied microstructures, and their varied hydrothermal alteration. As a result, the spatial distribution of the assembled volcanic materials is of paramount importance in deciphering fluid flow in active volcanic hydrothermal systems. To this end, we have constructed a cartoon cross section in which we capture the salient features of our study, presented as Fig. 18.

The chief lithologies at Whakaari are tuffs, lavas and lava breccias, and crater-filling un lithified tephra (Figs. 2, 3, and 18). The crater-filling tephra has a relatively high permeability ($\sim 10^{-15}$ to $\sim 10^{-12}$ m²), and is therefore unlikely to impede the movement of fluids within the shallow crater (Fig. 18, item 1), as evidenced by crater floor gas flux measurements (Bloomberg et al., 2014). Permeability in these un lithified deposits may also be enhanced by vertical gas elutriation pipes (Fig. 4c; Fig. 18, item 2). However, we highlight that bedding-induced permeability anisotropy (Supplementary Figs. S8–S11; Fig. 18, item 3) and well-sorted layers of fine ash with a low permeability (WI28 $\sim 10^{-19}$ m²; Fig. 3h and i; Fig. 18, item 4) may impede and prevent vertical fluid movement, respectively. We also note that permeability to gases will likely decrease with depth (in the first few meters) in the un lithified crater-fill due to the increase in water content, and therefore decrease in air-filled porosity, as depth increases (Figs. 8 and 9). While mineralogical transformations are unlikely to influence porosity and permeability (Fig. 17), cementation or clay formation will likely result in reductions in tephra permeability. In particular, cementation of near-vent tephra with sulphur (Fig. 3e and f), where the pH is too high for alunite precipitation (Giggenbach et al., 2003), results in the destruction of porosity and permeability, both horizontally as subcrater layers (Christenson et al., 2016) and vertically as fumaroles (sulphur flow sample WI29 contains a porosity of ~ 0.01 and a permeability $<10^{-18}$ m²; Fig. 18, item 5). Near-vent cementation of tephra and tuffs with sulphur could therefore lead to the clogging of active vents or time-variable prevention of lateral and/or vertical fluid movement (see also Harris and Maciejewski, 2000; Mayer et al., 2016b; Christenson et al., 2016).

The tuffs—formed by the consolidation and cementation of tephra deposits—are typically porous (porosity = 0.3–0.7), although their permeability can range from $\sim 10^{-17}$ to $\sim 10^{-12}$ m² (Fig. 15). Tuffs are found forming the crater wall (although the dominant lithology is lava/lava breccia; Figs. 2, 3, and 18) and presumably comprises the deep main crater fill (Fig. 18), as can be seen in ballistics from recent eruptions. As for the crater-fill tephra, bedding-induced permeability anisotropy and well-sorted layers of fine ash tuff with a very low permeability may impede or restrict the vertical movement of fluids (Fig. 18, item 6) and vertical gas elutriation pipes may assist vertical fluid movement (Fig. 18, item 4). A notable observation is that the white-coloured ash tuffs (an alteration colour associated with alunite) contain the lowest porosities and have the lowest permeabilities (Fig. 15). Therefore, hydrothermal alteration of the ash tuffs in shallow zones (alunite is formed through the oxidation of H₂S from deeper boiling fluids) that host or have hosted acid-sulphate hydrothermal fluids can result in reductions in porosity and permeability through the precipitation of pore-filling alunite (Fig. 18, item 7), providing that the fluid temperature and composition (including pH) support mineral precipitation. Hydrothermal alteration deeper in the crater could also result in modifications to permeability (e.g., dissolution, clay formation, amongst others; Fig. 18, item 8).

The crater walls chiefly comprise lavas and lava breccias (Figs. 2 and 3). Discontinuities at the crater margin serve as a passageway for hydrothermal fluids and feed the numerous active fumaroles, boiling mud pools, and springs for acid streams (Figs. 2, 3, and 16a; Fig. 18, item 9) (Bloomberg et al., 2014). The porosity of the lavas and lava breccias at Whakaari ranges from ~ 0.05 up to ~ 0.7 , and permeability ranges from $\sim 10^{-16}$ to $\sim 10^{-12}$ m² (Fig. 15). Notably, we find that (1) the lava

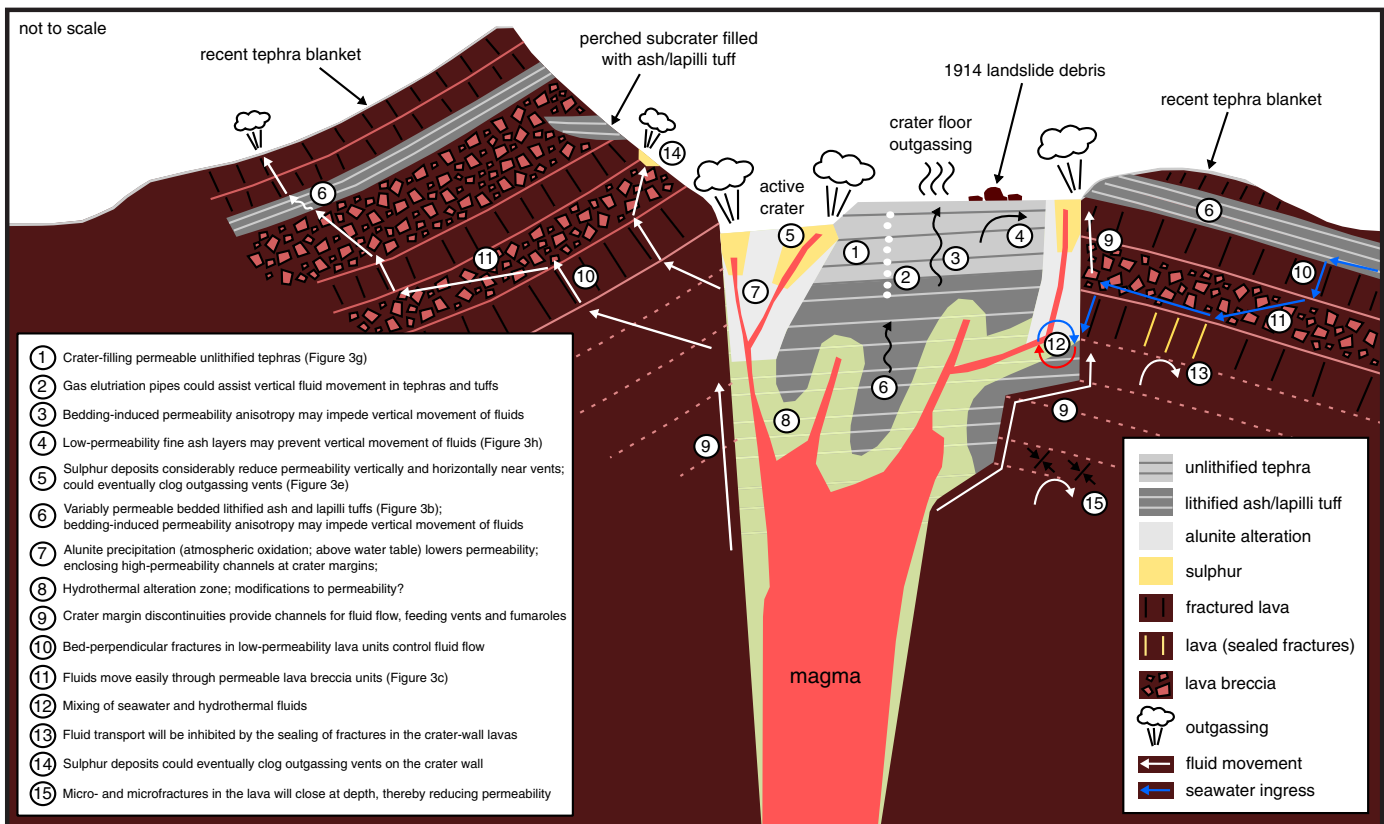


Fig. 18. Cartoon cross section of Whakaari from west-northwest to east-southeast (not to scale) that captures the salient features of our study. See text for details.

breccias are significantly more permeable than the coherent lavas (Fig. 15) and, (2) macroscopic fractures within the lava samples (Fig. 16a) increase sample permeability by up to three orders of magnitude (Fig. 15; Supplementary Table S4). As a result, fluids travelling through the crater walls (hydrothermal fluids and seawater; Fig. 18) will likely negotiate through a combination of fractures within the lava (Fig. 18, item 10) and the permeable lava breccia (Fig. 18, item 11). The ingress of seawater into the hydrothermal system will result in the mixing of hydrothermal fluids and seawater (Fig. 18, item 12). While the passage of hydrothermal fluids can weaken the lava and promote the growth and widening of fractures through alteration (e.g., mineral replacement and/or dissolution; Fig. 16a), hydrothermal fluids can also seal fractures through precipitation (Fig. 16b; Hedenquist et al., 1993). In zones where precipitation dominates over dissolution (a function of the fluid temperature and composition, including pH), the sealing of fractures will significantly reduce permeability (Griffiths et al., 2016; Fig. 18, item 13), transforming a zone of high-permeability into a zone of low-permeability. The mixing of hydrothermal fluids and seawater can also result in mineral precipitation (such as anhydrite) and reductions to permeability (Kawada and Yoshida, 2010). Fracture pathways within the crater wall may also become clogged with sulphur precipitation (Fig. 18, item 14). Finally, our data have shown that an increase in effective pressure (i.e., depth) will significantly reduce the permeability of the microfractured lava (Fig. 12). The permeability of macrofractures will also be reduced at depth (Nara et al., 2011). As a result, fluids may find it increasingly difficult to find an escape route into the crater wall as depth is increased (Fig. 18, item 15).

As outlined above, hydrothermal alteration typical of a volcanic hydrothermal system can result in increases (due to alteration-induced weakening and fracturing) and decreases (due to hydrothermal precipitation) to permeability. Importantly, a decrease in permeability, be it due to fracture sealing in the lava, pore-filling alunite precipitation, cementation by sulphur, and/or very low permeability layers (Fig. 18), can

result in pore pressure augmentation (Christenson et al., 2010; Heap and Wadsworth, 2016). An increase in pore pressure could jeopardise the stability of the volcanic slopes (Day, 1996; Voight and Elsworth, 1997; Reid et al., 2001; Reid, 2004; Moon et al., 2009), result in seismicity (Nishi et al., 1996; Sherburn et al., 1998; Chardot et al., 2015), and/or drive the wide variety of eruptions observed at Whakaari (e.g., Houghton and Nairn, 1991; Mayer et al., 2015). Indeed, an increase in pore pressure due to the hydrothermal system was thought responsible for the unrest between 2002–2006 and 2007–2009 (Fournier and Chardot, 2012), although we note that lake level variations are likely to have significantly modified the pore fluid pressure within the system during these intervals (Christenson et al., 2016).

The reduction in permeability may also encourage changes to the preferred pathways for hydrothermal fluid circulation. This is exemplified by the numerous past and present vents, fumaroles, and craters that pepper the main crater floor and the base of the slopes of the volcanic amphitheatre at Whakaari (Figs. 2 and 3) and highlights the constantly evolving and unpredictable nature of hydrothermal volcanic systems (see also Harris and Maciejewski, 2000). Changes to hydrothermal circulation will also expose new tephra and tuffs to alunite, clay, and sulphur alteration/precipitation. The exposure of new materials to porosity and permeability reducing alteration could therefore result in a reduction of the equivalent permeability of the system over time, thereby increasing the potential for pore pressure augmentation and the associated hazardous consequences.

The primary goal of this contribution was to produce a very large dataset to inform future modelling efforts. The permeability of the materials within active volcanic hydrothermal systems is, for example, required to understand and accurately model the outgassing of magmatic volatiles from the magma-filled conduit (Collombet, 2009; Collinson and Neuberg, 2012), subsurface hydrothermal activity and therefore volcanic unrest (Hurwitz et al., 2007; Peltier et al., 2009; Tedesco et al., 2010; Christenson et al., 2010; Fournier and Chardot, 2012), gas

monitoring (Bloomberg et al., 2014; Peiffer et al., 2014), and volcano seismicity (Leet, 1988; Nishi et al., 1996; Sherburn et al., 1998; Bean et al., 2014; Chardot et al., 2015). For example, Fournier and Chardot (2012) show, using a thermo-poro-elastic model, that increases in pore pressure at depth were likely responsible for recent (2002–2006 and 2007–2009) episodes of ground deformation at Whakaari. The model of Fournier and Chardot (2012) assumes an isotropic value permeability of 10^{-15} m^2 and, while these authors concede that the assumption of a permeability isotropy is an oversimplification, our study—which shows that permeability spans eight orders of magnitude (from $\sim 10^{-19}$ to $\sim 10^{-11} \text{ m}^2$) and is complicated by numerous spatial and temporal considerations (summarised in Fig. 18)—highlights the challenge presented for the construction of more complex models. Further, we stress that the construction of such models will require an improved understanding of the subsurface stratigraphy, hydrogeology, and geochemical composition of the hydrothermal fluids at Whakaari.

Our study provides the most comprehensive dataset for the porosity and permeability of the materials that comprise a volcanic hydrothermal system to date. Although our study highlights an extreme variability in these parameters, we anticipate that these data will allow for a better understanding of the behaviour and evolution of volcanic hydrothermal systems worldwide.

Author contributions

M.J. Heap led the project and wrote the manuscript. Field work and sample collection was carried out by M.J. Heap, B.M. Kennedy, J.I. Farquharson, K. Mayer, M. Letham-Brake, B. Scheu, Y. Lavallée, and P. Siratovich. Laboratory measurements of permeability were collected and analysed by J.I. Farquharson, M.J. Heap, and T. Reuschlé. The permeability at different confining pressures was performed and analysed by T. Reuschlé. J. Ashworth and J.I. Farquharson collected and analysed the field data for the lithified rocks. K. Mayer and B. Scheu collected the field data for the unlithified deposits, which was analysed by K. Mayer. H.A. Gilg gathered and analysed all of the XRPD data. M.J. Heap and B.M. Kennedy conducted the SEM work. J.I. Farquharson performed the Bayesian Information Criterion (BIC) analysis. The cross section was constructed by B.M. Kennedy, with help from M.J. Heap. All authors had a hand in the interpretation of the data and the writing of the manuscript.

Acknowledgements

The authors of this study acknowledge two Hubert Curien Partnership (PHC) grants: a Dumont d'Urville grant (number 31950RK) and a Procope grant (number 332065SG) funded and implemented by the New Zealand Ministry of Business, Innovation and Employment (MBIE), the Royal Society of New Zealand, the Deutscher Akademischer Austauschdienst (DAAD) in Germany, and the Ministry of Foreign Affairs (MAEDI) and the Ministry of Higher Education and Research (MENESR) in France. The first and third authors also acknowledge funding from an Initiative d'Excellence (IDEX) "Attractivité" grant (VOLPERM) and "Contrats doctoraux" grant, respectively, both funded by the University of Strasbourg. We acknowledge Catalyst Fund project "Energy straight from magma", funded and implemented by the Royal Society of New Zealand and the New Zealand Ministry of Business, Innovation and Employment (MBIE). Funding for B. Kennedy was additionally provided by Marsden Fast Start (09-UO-017C) grant. B. Kennedy and Y. Lavallée thank the international science linkage funds from Royal Society of New Zealand (ISAT E613), the German Aerospace Centre (DLR) and the Federal Ministry of Education and Research (BMBF) (NZA 09/17). D. B. Dingwell acknowledges the ERC advanced grant "EVOLES" (explosive volcanism in the earth system: experimental insights, project number 247076). B. Scheu and K. Mayer acknowledge funding from the European Union's Seventh Program for research, technological development, and demonstration under grant agreement No

282759 (VUELCO). Y. Lavallée acknowledges ERC starting grant "SLiM" (Strain Localisation in Magmas, project number 306488). The mercury porosimetry was performed at the University of Aberdeen and thanks go to Dave Healy and Colin Taylor. We gratefully acknowledge B. Scott, S. Bloomberg, A. Mazot, and N. Win for field assistance. The Buttle Family, Pee Jay Tours, and the New Zealand Royal Air Force, in conjunction with GNS Science, provided field access. Gilles Morvan is thanked for SEM assistance and Alexandra Kushnir for grammatical assistance. The comments of two anonymous reviewers improved the clarity of this manuscript.

Appendix A. Supplementary data

Supplementary data to this article can be found online at <http://dx.doi.org/10.1016/j.jvolgeores.2016.12.004>.

References

- Ball, J.L., Stauffer, P.H., Calder, E.S., Valentine, G.A., 2015. The hydrothermal alteration of cooling lava domes. *Bull. Volcanol.* 77 (102).
- Barberi, F., Bertagnini, A., Landi, P., Principe, C., 1992. A review on phreatic eruptions and their precursors. *J. Volcanol. Geotherm. Res.* 52, 231–246.
- Bean, C.J., De Barros, L., Lokmer, I., Métaxian, J.-P., O'Brien, G., Murphy, S., 2014. Long-period seismicity in the shallow volcanic edifice formed from slow-rupture earthquakes. *Nat. Geosci.* 7, 71–75.
- Bergmann, J., Friedel, P., Kleeburg, R., 1998. BGMN—a new fundamental parameters based Rietveld program for laboratory X-ray sources, its use in quantitative analysis and structure investigations. *CPD. Newsletter* 20, 5–8.
- Bertagnini, A., Landi, P., Santacroce, R., Sbrana, A., 1991. The 1906 eruption of Vesuvius: from magmatic to phreatomagmatic activity through the flashing of a shallow depth hydrothermal system. *Bull. Volcanol.* 53, 517–532.
- Bibby, H.M., Caldwell, T.G., Davey, F.J., Webb, T.H., 1995. Geophysical evidence on the structure of the Taupo Volcanic Zone and its hydrothermal circulation. *J. Volcanol. Geotherm. Res.* 68, 29–58.
- Bloomberg, S., Werner, C., Rissmann, C., Mazot, A., Horton, T., Gravely, D., Kennedy, B.M., Oze, C., 2014. Soil CO₂ emissions as a proxy for heat and mass flow assessment, Taupo Volcanic Zone, New Zealand. *Geochem. Geophys. Geosyst.* 15, 4885–4904.
- Bourbié, T., Zinszner, B., 1985. Hydraulic and acoustic properties as a function of porosity in Fontainebleau Sandstone. *J. Geophys. Res.* 90, 11524–11532.
- Brace, W.F., 1984. Permeability of crystalline rocks: new in situ measurements. *J. Geophys. Res.* 89, 4327–4330.
- Brace, W.F., Walsh, J.B., Frangos, W.T., 1968. Permeability of granite under high pressure. *J. Geophys. Res.* 73, 2225–2236.
- Browne, P.R.L., 1978. Hydrothermal alteration in active geothermal fields. *Annu. Rev. Earth Planet. Sci.* 6, 229–250.
- BS5930, 1999. *Code of Practice for Site Investigations*. British Standards Institution, London.
- Chardot, L., Jolly, A.D., Kennedy, B.M., Fournier, N., Sherburn, S., 2015. Using volcanic tremor for eruption forecasting at White Island volcano (Whakaari), New Zealand. *J. Volcanol. Geotherm. Res.* 302, 11–23.
- Christenson, B.W., 2000. Geochemistry of fluids associated with the 1995–1996 eruption of Mt. Ruapehu, New Zealand: signatures and processes in the magmatic-hydrothermal system. *J. Volcanol. Geotherm. Res.* 97, 1–30.
- Christenson, B.W., Reyes, A.G., Young, R., Moebis, A., Sherburn, S., Cole-Baker, J., Britten, K., 2010. Cyclic processes and factors leading to phreatic eruption events: insights from the 25 September 2007 eruption through Ruapehu Crater Lake, New Zealand. *J. Volcanol. Geotherm. Res.* 191, 15–32.
- Christenson, B.W., White, S., Britten, K., Scott, B.J., Mazot, A., 2016. *Hydrological Evolution and Chemical Structure of a Hyper-acidic Spring-lake System on White Island, New Zealand* (in review).
- Clark, R.H., Cole, J.W., 1986. White Island. Late Cenozoic Volcanism in New Zealand 23, pp. 169–178.
- Clauser, C., 1992. Permeability of crystalline rocks. *Earth Space Sci. News* 73, 233–238.
- Cole, J.W., Thordarson, T., Burt, R.M., 2000. Magma origin and evolution of White Island (Whakaari) Volcano, Bay of Plenty, New Zealand. *J. Petrol.* 41 (6), 867–895.
- Collinson, A.S.D., Neuberg, J., 2012. Gas storage, transport and pressure changes in an evolving permeable volcanic edifice. *J. Volcanol. Geotherm. Res.* 243–244, 1–13.
- Collombet, M., 2009. Two-dimensional gas loss for silicic magma flows: toward more realistic numerical models. *Geophys. J. Int.* 177, 309–318.
- Day, S.J., 1996. Hydrothermal pore fluid pressure and the stability of porous, permeable volcanoes. *Geol. Soc. Lond. Spec. Publ.* 110, 77–93.
- Deino, A.L., Orsi, G., De Vita, S., Piochi, M., 2004. The age of the Neapolitan Yellow Tuff caldera-forming eruption (Campi Flegrei caldera - Italy) assessed by ⁴⁰Ar/³⁹Ar dating method. *J. Volcanol. Geotherm. Res.* 133, 157–170.
- del Potro, R., Hürlimann, M., 2009. The decrease in the shear strength of volcanic materials with argillic hydrothermal alteration, insights from the summit region of Teide stratovolcano, Tenerife. *Eng. Geol.* 104, 135–143.
- Donachie, S.P., Christenson, B.W., Kunkel, D.D., Malahoff, A., Alam, M., 2002. Microbial community in acidic hydrothermal waters of volcanically active White Island, New Zealand. *Extremophiles* 6, 419–425.

- Ece, Ö.I., Schroeder, P.A., Smilley, M.J., Wampler, J.M., 2008. Acid-sulphate hydrothermal alteration of andesitic tuffs and genesis of halloysite and alunite deposits in the Biga Peninsula, Turkey. *Clay Miner.* 43, 281–315.
- Edmonds, M., Oppenheimer, C., Pyle, D.M., Herd, R.A., Thompson, G., 2003. SO₂ emissions from Soufrière Hills Volcano and their relationship to conduit permeability, hydrothermal interaction and degassing regime. *J. Volcanol. Geotherm. Res.* 124, 23–43.
- Eichelberger, J.C., Carrigan, C.R., Westrich, H.R., Price, P.H., 1986. Non-explosive silicic volcanism. *Nature* 323, 598–602.
- Farquharson, J.I., Heap, M.J., Varley, N., Baud, P., Reuschlé, T., 2015. Permeability and porosity relationships of edifice-forming andesites: a combined field and laboratory study. *J. Volcanol. Geotherm. Res.* 297, 52–68.
- Farquharson, J.I., Heap, M.J., Lavallée, Y., Baud, P., 2016. Evidence for the development of permeability anisotropy in lava domes and volcanic conduits. *J. Volcanol. Geotherm. Res.* 323, 163–185.
- Faulkner, D.R., Rutter, E., 2000. Comparisons of water and argon permeability in natural clay-bearing fault gouge under high pressure at 20 °C. *J. Geophys. Res.* 105 (B7), 16415–16426.
- Fournier, N., Chardot, L., 2012. Understanding volcano hydrothermal unrest from geodetic observations: insights from numerical modeling and application to White Island volcano, New Zealand. *J. Geophys. Res.* 117 (B11). <http://dx.doi.org/10.1029/2012JB009469>.
- Frolova, J., Ladygin, V., Rychagov, S., Zukhubaya, D., 2014. Effects of hydrothermal alterations on physical and mechanical properties of rocks in the Kuril–Kamchatka island arc. *Eng. Geol.* 183, 80–95.
- Giggenbach, W.F., Shinohara, H., Kusakabe, M., Obba, T., 2003. Formation of acid volcanic brines through interaction of magmatic gases, seawater, and rock within the White Island volcanic-hydrothermal system, New Zealand. *Spec. Publ. Soc. Econ. Geol.* 10, 19–40.
- Griffiths, L., Heap, M.J., Wang, F., Daval, D., Gilg, H.A., Baud, P., Schmittbuhl, J., Genter, A., 2016. Geothermal implications for fracture-filling hydrothermal precipitation. *Geothermics* <http://dx.doi.org/10.1016/j.geothermics.2016.06.006>.
- Harris, A.J.L., Maciejewski, A.J.H., 2000. Thermal surveys of the Vulcano Fossa fumarole field 1994–1999: evidence for fumarole migration and sealing. *J. Volcanol. Geotherm. Res.* 102, 119–147.
- Heap, M.J., Kennedy, B.M., 2016. Exploring the scale-dependent permeability of fractured andesite. *Earth Planet. Sci. Lett.* 447, 139–150.
- Heap, M.J., Wadsworth, F.B., 2016. Closing an open system: pore pressure changes in permeable edifice rock at high strain rates. *J. Volcanol. Geotherm. Res.* 315, 40–50.
- Heap, M.J., Lavallée, Y., Petráková, L., Baud, P., Reuschlé, T., Varley, N., Dingwell, D.B., 2014. Microstructural controls on the physical and mechanical properties of edifice-forming andesites at Volcán de Colima, Mexico. *J. Geophys. Res.* 119, 2925–2963.
- Heap, M.J., Farquharson, I.J., Wadsworth, F.B., Kolzenburg, S., Russell, J.K., 2015a. Time-scales for permeability reduction and strength recovery in densifying magma. *Earth Planet. Sci. Lett.* 429, 223–233.
- Heap, M.J., Kennedy, B.M., Pernin, N., Jacquemard, L., Baud, P., Farquharson, I.J., Scheu, B., Lavallée, Y., Gilg, H.A., Letham-Brake, M., Mayer, K., Jolly, A.D., Reuschlé, T., Dingwell, D.B., 2015b. Mechanical behaviour and failure modes in the Whakaari (White Island volcano) hydrothermal system, New Zealand. *J. Volcanol. Geotherm. Res.* 295, 26–42.
- Hedenquist, J.W., Simmons, S.P., Giggenbach, W.F., Eldridge, C.S., 1993. White Island, New Zealand, volcanic-hydrothermal system represents the geochemical environment of high-sulfidation Cu and Au ore deposition. *Geology* 21, 731–734.
- Houghton, B.F., Nairn, I.A., 1989. The 1976–82 eruption sequence at White Island volcano (Whakaari), Bay of Plenty, New Zealand. *NZ Geol. Surv. Bull.* 103, 1–136.
- Houghton, B.F., Nairn, I.A., 1991. The 1976–1982 Strombolian and phreatomagmatic eruptions of White Island, New Zealand: eruptive and depositional mechanisms at a 'wet' volcano. *Bull. Volcanol.* 54, 25–49.
- Hurwitz, S., Christiansen, L.B., Hsieh, P.A., 2007. Hydrothermal fluid flow and deformation in large calderas: inferences from numerical simulations. *J. Geophys. Res.* 112, B02206. <http://dx.doi.org/10.1029/2006JB004689>.
- Inoue, A., 1995. Formation of clay minerals in hydrothermal environments. In: Velde, B. (Ed.), *Origin and Mineralogy of Clays*. Springer, Berlin, pp. 268–329.
- Jaupart, C., 1998. Gas loss from magmas through conduit walls during eruption. *Geol. Soc. Lond. Spec. Publ.* 145, 73–90.
- Johnston, J.H., 1977. Jarosite and akaganéite from White Island volcano, New Zealand: an X-ray and Mössbauer study. *Geochim. Cosmochim. Acta* 41, 539–544.
- Jolly, A., Kennedy, B.M., Edwards, M., Jousset, P., Scheu, B., 2016. Infrasound tremor from bubble burst eruptions in the viscous shallow crater lake of White Island, New Zealand, and its implications for interpreting volcanic source processes. *J. Volcanol. Geotherm. Res.* 327, 585–603.
- Kaneshima, S., Kawakatsu, H., Matsubayashi, H., Sudo, Y., Tsutsui, T., Ohminato, T., Ito, H., Ubara, K., Yamamoto, H., Okawa, J., Takeo, M., Iidaka, T., 1996. Mechanism of phreatic eruptions at Aso volcano inferred from near-field broadband seismic observations. *Science* 273, 642.
- Kawada, Y., Yoshida, S., 2010. Formation of a hydrothermal reservoir due to anhydrite precipitation in an arc volcano hydrothermal system. *J. Geophys. Res.* 115 (B11106). <http://dx.doi.org/10.1029/2010JB007708>.
- Kendrick, J.E., Lavallée, Y., Varley, N., Wadsworth, F.B., Lamb, O.D., Vasseur, J., 2016. Blowing off steam: tuffsite formation as a regulator for lava dome eruptions. *Front. Earth Sci.* <http://dx.doi.org/10.3389/feart.2016.00041>.
- Kennedy, B., Wadsworth, F.B., Vasseur, J., Schipper, C.I., Jellinek, A.M., von Aulock, F.W., Hess, K.-U., Russell, J.K., Lavallée, Y., Nichols, A.R.L., Dingwell, D.B., 2016. Surface tension driven processes densify and retain permeability in magma and lava. *Earth Planets Sci. Lett.* 433, 116–124.
- Klinkenberg, L.J., 1941. The permeability of porous media to liquids and gases, drilling and production. *Practice* 200–213.
- Klug, C., Cashman, K.V., 1996. Permeability development in vesiculating magmas: implications for fragmentation. *Bull. Volcanol.* 58, 87–100.
- Kueppers, U., Scheu, B., Spieler, O., Dingwell, D.B., 2005. Field-based density measurements to tool to identify preeruption dome structure: set-up and first results from Unzen volcano, Japan. *J. Volcanol. Geotherm. Res.* 141, 65–75.
- Kushnir, A.R.L., Martel, C., Bourdier, J.-L., Heap, M.J., Reuschlé, T., Erdmann, S., Komorowski, J.C., Cholik, N., 2016. Probing permeability and microtexture: unravelling the role of a low-permeability dome on the explosivity of Merapi (Indonesia). *J. Volcanol. Geotherm. Res.* 316, 56–71.
- Leet, R.C., 1988. Saturated and subcooled hydrothermal boiling in groundwater flow channels as a source of harmonic tremor. *J. Geophys. Res.* 93, 4835–4849.
- Main, I.G., Leonard, T., Papasouliotis, O., Hatton, C.G., Meredith, P.G., 1999. One slope or two? Detecting statistically significant breaks of slope in geophysical data, with application to fracture scaling relationships. *Geophys. Res. Lett.* 26, 2801–2804.
- Mayer, K., Scheu, B., Gilg, H.A., Heap, M.J., Kennedy, B.M., Lavallée, Y., Letham-Brake, M., Dingwell, D.B., 2015. Experimental constraints on phreatic eruption processes at Whakaari (White Island volcano). *J. Volcanol. Geotherm. Res.* 302, 150–162.
- Mayer, K., Scheu, B., Montanaro, C., Yilmaz, T.I., Isaia, R., Aßbichler, D., Dingwell, D.B., 2016a. Hydrothermal alteration of surficial rocks at Solfatara (Campi Flegrei): petrophysical properties and implications for phreatic eruption processes. *J. Volcanol. Geotherm. Res.* 320, 128–143.
- Mayer, K., Scheu, B., Rott, S., Montanaro, C., Yilmaz, T.I., Gilg, H.A., Joseph, E.P., Dingwell, D.B., 2016b. Phreatic activity and hydrothermal alteration in the Valley of Desolation, Dominica. *Bull. Volcanol.* (in review).
- Mongillo, M.A., Wood, C.P., 1995. Thermal infrared mapping of White Island volcano, New Zealand. *J. Volcanol. Geotherm. Res.* 69, 59–71.
- Montanaro, C., Scheu, B., Gudmundsson, M.T., Vogfjörd, K., Reynolds, H.I., Dürig, T., Strehlow, K., Rott, S., Reuschlé, T., Dingwell, D.B., 2016. Multidisciplinary constraints of hydrothermal explosions based on the 2013 Gengissig lake events, Kverkfjöll volcano, Iceland. *Earth Planet. Sci. Lett.* 434, 308–319.
- Moon, V., Bradshaw, J., de Lange, W., 2009. Geomorphic development of White Island Volcano based on slope stability modelling. *Eng. Geol.* 104, 16–30.
- Mueller, S., Melnik, O., Spieler, O., Scheu, B., Dingwell, D.B., 2005. Permeability and degassing of dome lavas undergoing rapid decompression: an experimental study. *Bull. Volcanol.* 67, 526–538.
- Mutlu, H., Sarıiz, K., Kadir, S., 2005. Geochemistry and origin of the Şaphane alunite deposit, Western Anatolia, Turkey. *Ore Geol. Rev.* 26, 39–50.
- Nara, Y., Meredith, P.G., Yoneda, T., Kaneko, K., 2011. Influence of macro-fractures and micro-fractures on permeability and elastic wave velocities in basalt at elevated pressure. *Tectonophysics* 503, 52–59.
- Neuman, S.P., 1994. Generalized scaling of permeabilities: validation and effect of support scale. *Geophys. Res. Lett.* 21, 349–352.
- Nishi, Y., Sherburn, S., Scott, B.J., Sugihara, M., 1996. High-frequency earthquakes at White Island volcano, New Zealand: insights into the shallow structure of a volcano-hydrothermal system. *J. Volcanol. Geotherm. Res.* 72, 183–197.
- Pfeiffer, L., Bernard-Romero, R., Mazot, A., Taras, Y.A., Guevara, M., Santoyo, E., 2014. Fluid geochemistry and soil gas fluxes (CO₂-CH₄-H₂S) at a promissory Hot dry rock geothermal system: the Acoculco caldera, Mexico. *J. Volcanol. Geotherm. Res.* 284, 122–137.
- Peltier, A., Scott, B.J., Hurst, T., 2009. Ground deformation patterns at White Island volcano (New Zealand) between 1967 and 2008 deduced from levelling data. *J. Volcanol. Geotherm. Res.* 181, 207–218.
- Pirajno, F., 2009. *Hydrothermal Processes and Mineral Systems*. Springer, Netherlands, p. 1250.
- Pola, A., Crosta, G.B., Fusi, N., Barberini, V., Norini, G., 2012. Influence of alteration on physical properties of volcanic rocks. *Tectonophysics* 566–567.
- Pola, A., Crosta, G.B., Fusi, N., Castellanza, R., 2014. General characterization of the mechanical behaviour of different volcanic rocks with respect to alteration. *Eng. Geol.* 169, 1–13.
- Procter, J.N., Cronin, S.J., Zernack, A.V., Lube, G., Stewart, R.B., Nemeth, K., Keys, H., 2014. Debris flow evolution and the activation of an explosive hydrothermal system; Te Maari, Tongariro, New Zealand. *J. Volcanol. Geotherm. Res.* 286, 331–347.
- Reed, M.H., 1997. Hydrothermal alteration and its relationship to ore fluid composition. In: Barnes, H.L. (Ed.), *Geochemistry of Hydrothermal Ore Deposits*, third ed. Wiley, New York, pp. 303–366.
- Reid, M.E., 2004. Massive collapse of volcano edifices triggered by hydrothermal pressurization. *Geology* 32, 373–376.
- Reid, M.E., Sisson, T.W., Brien, D.L., 2001. Volcano collapse promoted by hydrothermal alteration and edifice shape, Mount Rainier, Washington. *Geology* 29, 779–782.
- Rowland, J.V., Sibson, R.H., 2004. Structural controls on hydrothermal flow in a segmented rift system, Taupo Volcanic Zone, New Zealand. *Geofluids* 4, 259–283.
- Rust, A., Cashman, K.V., 2004. Permeability of vesicular silicic magma: inertial and hysteresis effects. *Earth Planet. Sci. Lett.* 228, 93–107.
- Rye, R.O., Bethke, P.M., Wasserman, M.D., 2002. The stable isotope geochemistry of acid sulfate alteration. *Econ. Geol.* 87, 225–262.
- Saar, M.O., Manga, M., 1999. Permeability–porosity relationship in vesicular basalts. *Geophys. Res. Lett.* 26, 111–114.
- Schaefer, L.N., Kendrick, J.E., Oommen, T., Lavallée, Y., Chigna, G., 2015. Geomechanical rock properties of a basaltic volcano. *Front. Earth Sci.* 3:29. <http://dx.doi.org/10.3389/feart.2015.00029>.
- Selvadurai, A.P.S., Selvadurai, P.A., 2010. Surface permeability tests: experiments and modelling for estimating effective permeability. *Proc. Roy. Soc. A* 466. <http://dx.doi.org/10.1098/rspa.2009.0475>.
- Sherburn, S., Scott, B.J., Nishi, Y., Sugihara, M., 1998. Seismicity at White Island volcano, New Zealand: a revised classification and inferences about source mechanism. *J. Volcanol. Geotherm. Res.* 83, 287–312.

- Siratovich, P., Heap, M.J., Villeneuve, M.C., Cole, J.W., Reuschlé, T., 2014. Physical property relationships of the Rotokawa Andesite, a significant geothermal reservoir rock in the Taupo Volcanic Zone, New Zealand. *Geotherm. Energy* 2 (10). <http://dx.doi.org/10.1186/s40517-014-0010-4>.
- Steiner, A., 1968. Clay minerals in hydrothermally altered rocks at Wairakei, New Zealand. *Clay Clay Miner.* 16, 193–213.
- Tanikawa, W., Shimamoto, T., 2009. Comparison of Klinkenberg-corrected gas permeability and water permeability in sedimentary rocks. *Int. J. Rock Mech. Min. Sci.* 46, 229–238.
- Todesco, M., Rinaldi, A.P., Bonforte, A., 2010. Modeling of unrest signals in heterogeneous hydrothermal systems. *J. Geophys. Res.* 115, B09213. <http://dx.doi.org/10.1029/2010JB007474>.
- Vinciguerra, S., Trovato, C., Meredith, P.G., Benson, P.M., 2005. Relating seismic velocities, thermal cracking and permeability in Mt. Etna and Iceland basalts. *Int. J. Rock Mech. Min. Sci.* 42, 900–910.
- Voight, B., Elsworth, D., 1997. Failure of volcano slopes. *Geotechnique* 47, 1–31.
- Wadsworth, F.B., Vasseur, J., Scheu, B., Kendrick, J.E., Lavallée, Y., Dingwell, D.B., 2016. Universal scaling of fluid permeability during volcanic welding and sediment diagenesis. *Geology* 44, 219–222.
- Werner, C., Hurst, T., Scott, B.J., Sherburn, S., Christensen, B.W., Britten, K., Cole-Baker, J., Mullan, B., 2008. Variability of passive gas emissions, seismicity, and deformation during crater lake growth at White Island Volcano, New Zealand, 2002–2006. *J. Geophys. Res.* 113 (B1). <http://dx.doi.org/10.1029/2007JB005094>.
- Whitaker, S., 1996. The Forchheimer equation: a theoretical development. *Transp. Porous Media* 25, 27–61.
- Wright, H.M.N., Roberts, J.J., Cashman, K.V., 2006. Permeability of anisotropic tube pumice: Model calculations and measurements. *Geophys. Res. Lett.* 33. <http://dx.doi.org/10.1029/2006GRL027224>.
- Wright, H.M.N., Cashman, K.V., Gottesfeld, E.H., Roberts, J.J., 2009. Pore structure of volcanic clasts: measurements of permeability and electrical conductivity. *Earth Planet. Sci. Lett.* 280, 93–104.
- Wyering, L.D., Villeneuve, M.C., Wallis, I.C., Siratovich, P., Kennedy, B., Gravely, D.M., Cant, J.L., 2014. Mechanical and physical properties of hydrothermally altered rocks, Taupo Volcanic Zone, New Zealand. *J. Volcanol. Geotherm. Res.* 288, 76–93.
- Wyering, L.D., Villeneuve, M.C., Wallis, I.C., Siratovich, P., Kennedy, B.M., Gravely, D., 2015. The development and application of the alteration strength index equation. *Eng. Geol.* 199, 48–61.
- Zhu, W., Wong, T.-f., 1997. The transition from brittle faulting to cataclastic flow: permeability evolution. *J. Geophys. Res.* 102 (B2), 3027–3041.
- Zimbelman, D.R., Rye, R.O., Breit, G.N., 2005. Origin of secondary sulfate minerals on active andesitic stratovolcanoes. *Chem. Geol.* 215 (1), 37–60.